HIGH CAPACITY WIDEBAND CO-SITE CO-CHANNEL INTERFERENCE CANCELLATION SYSTEM FOR ENHANCING WIRELESS COMMUNICATIONS

by

QI ZHOU

(Under the Direction of Mable P. Fok)

ABSTRACT

A high capacity wideband co-site co-channel interference cancellation system (ICS), is proposed and experimentally demonstrated. The demonstrated cancellation system subtracts the in-band wideband interfering signal from the received signal, such that the weak signal of interest (SOI) can be recovered. Our approach takes the good parts of both an electrical and an optical system to achieve deep cancellation with wide operation bandwidth. This proposed architecture is capable of canceling both line of sight and multipath interference. A 30-dB cancellation over 5.5 GHz and more than 50-dB cancellation over 150 MHz are experimentally obtained. Furthermore, to enable dynamic co-site interference cancellation at GHz speed, a semiconductor-optical-amplifiers (SOA) based ultrafast tunable time delay has been developed and incorporated into the ICS. Lastly, a novel microwave photonic mixer is demonstrated using polarization rotation in SOA and can be employed as the front end of the ICS for enhancing wireless transmission capacity.

INDEX WORDS: Co-site co-channel interference cancellation, High-speed tunable delay, Microwave photonic mixer

HIGH CAPACITY WIDEBAND CO-SITE CO-CHANNEL INTERFERENCE CANCELLATION SYSTEM FOR ENHANCING WIRELESS COMMUNICATIONS

by

QI ZHOU

BE, University of Science and Technology of China, China, 2013

A Thesis Submitted to the Graduate Faculty

of The University of Georgia in Partial Fulfillment

of the

Requirements for the Degree

MASTER OF SCIENCE

ATHENS, GEORGIA

2015

HIGH CAPACITY WIDEBAND CO-SITE CO-CHNNEL INTERFERENCE CANCELLATION SYSTEM FOR ENHANCING WIRELESS COMMUNICATIONS

by

QI ZHOU

Major Professor: Mable P. Fok

Committee: Mark A. Haidekker
Peter Kner

Electronic Version Approved:

Suzanne Barbour
Dean of the Graduate School
The University of Georgia
August 2015

DEDICATION

TO

MY PARENTS

GONGDI ZHOU and MEIFENG QI

MY GIRLFRIEND

XI CHEN

FOR GIVING ME UNCONDITIONAL SUPPORT ALL THE TIME

ACKNOWLEDGEMENTS

I would like to express my greatest gratitude to my major professor, Dr. Mable P. Fok who mentored me in the past two years. I appreciate her encouragement and guidance to me which helped me to grow up from a student to a researcher. Without her efforts on the project, this thesis would not be fruitful.

I also would like to thank Dr. Peter Kner, Dr. Mark Haidekker and Dr. Gee-kung Chang who provide important suggestions for my projects.

I would like to express my appreciation to all my lab colleagues, Ryan Toole, Mary Locke, Amanda Nicole Stark, Guy Scott, Alex Mathews, Aneek Enrique James. Especially, I would like to thank Mr. Hanlin Feng and Mr. Jia Ge for their help during my fresh year.

Thank all my friends in UGA for their kind help and moral support.

Finally, I would like to acknowledge the funding support of National Science Foundation (Award number: CNS 1217435).

TABLE OF CONTENTS

Page

LIST OF TABLES

Page

LIST OF FIGURES

Page

CHAPTER 1

INTRODUCTION AND LITERATURE REVIEW

1.1 Background and Motivation

The broadcast nature of the wireless medium has facilitated a wide array of communication applications, including pervasive systems and remote sensing. However, the wireless medium also makes such systems particularly susceptible to radio interference. Interference problem becomes particularly significant when multiple transmitting and receiving antennas are placed on the same structure. This type of interference is called co-site interference or self-interference. Co-site interference is commonly found on high mobility multipurpose wheeled vehicle (Humvee), helicopter, or unmanned aerial vehicle (UAV) because multiple antennas are placed on each vehicle for the guidance, command and control systems, as illustrated in Figure 1.1. Co-site interference is severe because the interference from the adjacent transmitter is so strong compared with the weak signal of interest (SOI) that is being received, so that the SOI is completely masked by the strong interfering signal and the receiver is overwhelmed by the strong interferer. The situation is even worse if the interfering signal is in-band, which is referred as co-channel interference. Even a notch filter cannot remove the interfering signal because the weak SOI and the interfering signal are sharing the same frequency spectrum, as illustrated in Figure 1.1. Moreover, co-site co-channel interference prohibits effective spectral usage of the RF

spectral resources as well as full-duplex capability, which is particularly important in the overcrowded unregulated frequency bands [1].

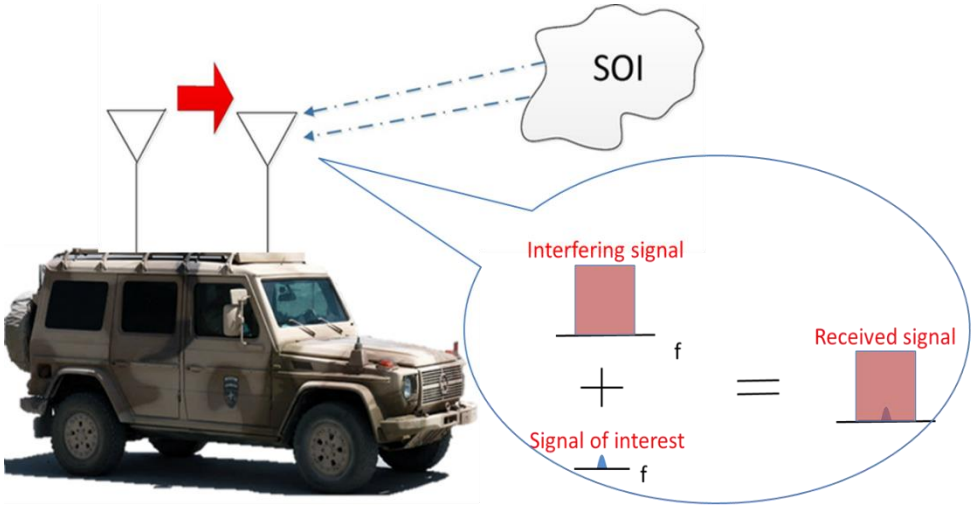

Figure 1.1. Illustration of a co-site co-channel interference scenario.

1.2 Objectives

As in co-site interference, since the interfering signal is our local transmitting signal, a copy of the interfering signal can be obtained. However, the remaining problem is how to efficiently cancel out the strong interference while recovering the weak SOI. The goals of the proposed system are listed below:

1. Wideband cancellation on both line of sight and multipath interference as well as fully recovery of weak SOI.
2. Fast adaptive to any changes in channel response.
3. Improve spectral efficiency and capacity of wireless communications.

1.3 Co-Site Co-Channel Interference Cancellation

This section will discuss exploring and characterizing existing approaches for co-site and co-channel interference cancellation system (ICS).

Interference Cancellation

To deal with the problem of co-site co-channel interference, researchers have put efforts on developments of different techniques and architectures. As mentioned above, co-site co-channel interference corresponds to the condition when the receiver is located near a strong transmitter and the transmitting and receiving signal share the same frequency band. This makes extracting or detecting a weak signal from the receiver extremely difficult. Related research and solutions have been conducted and discussed since 1980s. In the following subsections, we will go through the advantages and disadvantages of traditional electronics and optics based approaches, as well as the challenges that hinder further improvement of the cancellation performance.

Most of the co-site co-channel interference cancellation schemes are based on signal subtraction because of the knowledge on local transmitting signals. Those schemes consist of weight and delay to mimic channel response encountered by the interfering signal as well as signal inversion for interfering signal subtraction.

Traditional Electronics Approaches

There are two main categories of electronics-based interference cancellation which are analog and digital. Analog approaches directly work on the received and interfering signals without digitization; while digital approaches perform digital signal processing on both signals. The most commonly employed analog approach is the Quellan QHx220 chip [2]. This chip is typically integrated with the headset, cell phone and so on to combat the co-site interference between the inner antennas and improve the quality of the weak signal. This process is obtained through time sampling of the noise source and emulating the RF propagating channel between the transmitting and receiving antennas based on an active signal processing circuit. The cancellation signal can be emulated during this process. Moreover, in-phase and quadrature control voltages are used simultaneously to adjust the amplitude and phase of the cancellation signal. After applying the cancellation signal directly onto the receiving antenna, the interfering effects of noise sources surrounding the antenna can be effectively cancelled out. The QHx220 can achieve around 20-25 dB cancellation over a 10 MHz bandwidth. Its performance is limited by the constraints on input signal power as well as being limited to few modulation formats. The most commonly used interference mitigation technique for digital approaches is using matched filter because of its ability of channel estimation and compensation [3]. In this case, a pilot signal is transmitted to test the impulse response of the channel. Based on the impulse response, a matched filter is created to generate the inversion of the channel response using digital signal processing. This transversal filter approach is useful in canceling clutter and multi-path reflections in passive radar. This approach can achieve approximately 30 dB of

cancellation over a 10 MHz bandwidth. The narrow working bandwidth is limited by the bandwidth of electronic components, the sampling speed and the linearity of analog to digital converters. Besides, the best attempts among all electronics approaches only achieved a cancellation of 30 dB over 3-MHz bandwidth [4] for digital approaches and a cancellation of 30 dB over 35-MHz bandwidth [1] for analog approaches.

Combined analog-digital approach has also been explored by using an RF Balun transformer, an RF delay line, and an RF attenuator for analog cancellation, followed by digital cancellation for further enhancing the cancellation depth. A 45-dB cancellation over 40-MHz bandwidth is experimentally achieved [5] with the analog-digital approach. The cancellation depth and bandwidth of this approach are still limited by the bandwidth, linearity, precision of the electrical delay line and attenuator as well as the sampling speed and the linearity of analog to digital converter.

Optics-Based Interference Cancellation

Fiber optics has been well known for its ultra-broadband and high precision properties [6], which provide a promising alternative to electronic approaches. The attempts of optics based interference cancellation approaches can be dated back to the early 1990s, started from the work done by the MIT Lincoln Laboratory [7]. They try to design an optics-based interference cancellation technique to replace the inadequate channel-tracking capabilities of electronics based interference cancellers. Optics-based approach is promising, because the RF signal will only occupy a small fractional bandwidth after modulating onto the optical domain, allowing for precise channel tracking. The proposed nulling system

consists of switchable optical delay lines, along with a series of controllable complex optical weights to allow for tuning on phase and amplitude. However, the work was purely theoretical and the implementation into a practical system is extremely complex.

Recently, a much simpler implementation based on two counter-biased Mach-Zehnder intensity modulators (MZMs), tunable optical delay and attenuators is proposed [8]. Around 30-dB cancellation over 96-MHz bandwidth is experimentally demonstrated. However, its cancellation performance is limited by the S21 mismatch between the two MZMs. Another approach using electro-absorption modulators (EAMs) for electrical-to-optical (E-O) conversion, and a balanced photodetector for signal subtraction has been demonstrated later. This approach results in a significant improvement in cancellation bandwidth due to the better S21 matching between the EAMs, such that ~25 dB of cancellation over 400-MHz bandwidth is obtained experimentally [9]. Nevertheless, the balanced photodetector in use for signal subtraction is not adequate for analog signal inversion and limits the obtainable cancellation bandwidth.

System Characterization Standards

We have intensively studied and compared both electrical and optical approaches based on system characterization standards. These standards are efficient to evaluate both the electronics and optics based architecture for interference cancellation. These parameters consist of standard measures of performance on RF photonic links, as well as operating frequency, cancellation bandwidth, and depth of cancellation.

Link Loss

Link loss is defined by the loss introduced when a signal transmits through the link consisting of couplers, adapters, passive components, and electro-optic (EO) and optic-electro (OE) conversions. Compared with electrical based approaches, optics-based interference cancellation systems provide much less link loss. e.g 1-km fiber only introduces a 0.2-dB loss while 1 m of RF cable typically causes a 1-dB loss. The link loss in dB can be calculated by the following formula:

$$\text{Link Loss} = P_{\text{output, electrical}} - P_{\text{input, electrical}} \quad (1.1)$$

$P_{\text{input, electrical}}$ and $P_{\text{output, electrical}}$ represent the power of the input and output signal of the link in dBm. For optics-based approaches, a large portion of link loss is incurred at the EO and OE interface because of its dependency on electro-optics conversion.

Dynamic Range

Dynamic range describes the ratio between the largest and smallest possible signal strength of a given system. The required dynamic range for interference cancellation systems depends on signal strength of both the signal of interest and interfering signal. Also, the dynamic range will vary for different frequency bands of interest. To quantify the dynamic range, the spurious-free dynamic range (SFDR) is used for the measurements of interference cancellation system performance. SFDR is defined as two-thirds of the interval between the third-order intercept point (IIP_3) and the noise floor (P_N) in log scale and it refers to the difference between the minimum detectable signal and the maximum signal

that can be introduce into system [10]. In short, we need to measure the noise floor with 1 Hz of precision, the gain (G) of the whole system and then use the linear fit trend lines to calculate the third-order input intercept point. The SFDR is given by the formula below:

$$\text{SFDR}=\frac{2}{3}(IIP_3 + G - P_N) \quad (1.2)$$

An alternative SFDR measurement is given by the calculation of noise figure (NF):

$$\text{NF}= P_N - (-\text{BNL} + 10\log_{10}(\text{BW}) + \text{G}) \quad (1.3)$$

SFDR can also be expressed in terms of the IIP3, the background thermal noise (BNL) of -174 dBm/Hz, the system bandwidth (BW), and the NF, given as the equation below:

$$\text{SFDR} = \frac{2}{3}(IIP_3 - \text{BNL} - 10\log_{10}(\text{BW}) - \text{NF}) \quad (1.4)$$

Cancellation Performance Specifications

Operating frequency range, depth of cancellation, and cancellation bandwidth are all performance specifications for interference cancellation systems. Operating frequency range reflects the working frequency range of the interference canceller. Cancellation depth is a straightforward indicator for interference canceller's performance. It indicates the power reduction of the interferer using an interference cancellation system. Cancellation bandwidth is a trade-off to cancellation depth. The dispersive effects of electrical and optical components limit the interference cancellation performance to obtain a deep cancellation depth over broad bandwidth. The signal at different frequencies will experience different amounts of delay across the channel so that no single delay adjustment will compensate for the aggregate delay effects at various frequencies. The wider cancellation bandwidth with a deep cancellation depth will require the components in use

for the interferer canceller to have a better matched S21 response as well as an efficient model for redoing multipath effects.

The following tables summarize the current developments and approaches for co-site interference cancellation. Table 1.1 is comparing different interference approaches, while Table 1.2 is comparing different signal inversion (subtraction) approaches, which is an essential part for the performance of interference cancellation.

Table 1.1. Comparison of different interference cancellation approaches.

	Bandwidth	**Operating frequency**	**Cancellation Depth**	**Major Limitation**
QHx220 (Active Isolation Enhancer and Interference Canceler)[2]	10MHz	300MHz to 3GHz	20-25 dB	Limited input signal power
Balanced and unbalanced Transformer [5]	40MHz	Center Frequency at 2.45GHz	45 dB for 40 MHz 73dB for a 10MHz OFDM signal with cancellation in digital domain	Delay and attenuation is done using electronics with strong bandwidth limitation
Matched Filter (electronics) [3]	10MHz	88-108MHz	30 dB	Bandwidth limitation
Nulling antenna System (optical) [7]	2GHz	Center Frequency at 6 GHz	40 dB null depth	Theoretical work, real system is complex
Coherent OCS [10]	1GHz	0.25 to 4 GHz	20dB for broadband cancellation 60dB for narrowband cancellation	Limited Bandwidth and coarse granularity of electrical delay and attenuation adjustments

Direct Modulation [10]	1GHz	500 MHz	40dB for broadband cancellation 75dB for narrowband cancellation	Much lower third order input intercept point (IIP3). Mainly work for low-power signal. Modulation speed of the laser diode limits the operation frequency.
Incoherent OCS(MZM) [8]	1GHz	3 GHz	25dB for 1GHz broadband cancellation. 70dB for narrowband cancellation 40dB over 200MHz,50dB over 10MHz with broadband multipath cancellation	Frequency response mismatch between two MZMs in the system.
Incoherent OCS(EAM) [9]	40MHz	900MHz and 2.4GHz	30dB for broadband cancellation 65dB for narrowband cancellation	EAM is relatively expensive, not adequate analog signal inversion based on balanced PD

Table 1.2. Comparison of different signal inversion approaches.

	SFDR	Operating frequency Range	Major Limitation
Balanced and unbalanced Transformer [5]	More than 90dBm/Hz$^{2/3}$	200kHz to 10 GHz, Potential for future broadband use	Not enough isolation between output ports
Cross-Gain Modulation [11]	25-65dBm/Hz	Up to 10 GHz	Dynamic range is small
Opposite biased Modulator [8]	83dBm/Hz	Up to 10 GHz	Dynamic range is small
Balanced photodetector [9]	105dBm/Hz	Up to 20 GHz	Active device, not adequate signal inversion

Design Consideration

Decent cancellation over a broad bandwidth relies on the high precision of the optical delay line and attenuator as well as the small S21 mismatch. The optical delay and attenuator have a precision of 0.03 ps and 4×10^{-4} dB, respectively, while the best precision of electrical delays and attenuators are more than 6 ps and 0.001 dB. Higher precision on

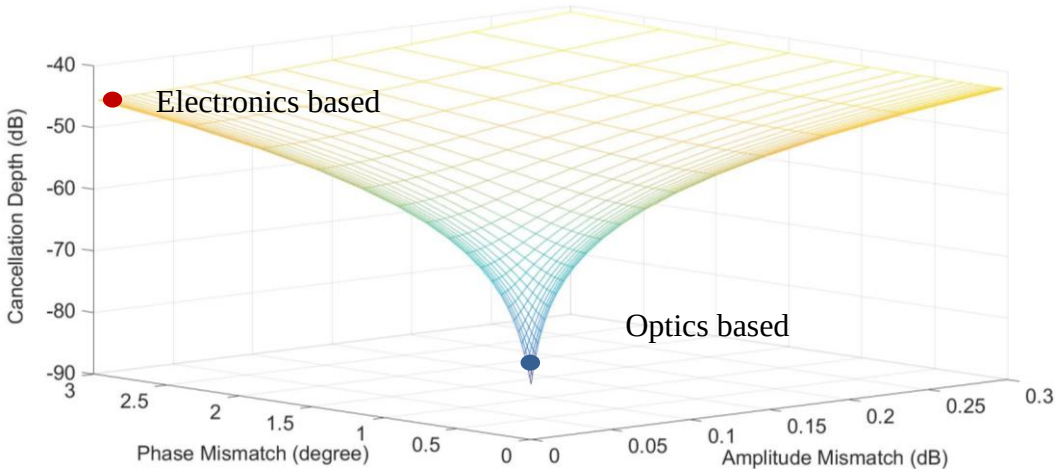

Figure 1.2. Simulation of cancellation depth over amplitude and phase mismatch.

delay and attenuation contribute to less mismatch on phase and amplitude. Figure 2.1 is the simulation result which indicates the cancellation depth over phase and amplitude mismatch. By mapping corresponding value of optical and electrical approach to the plot, it's easy to find the optical approach is able to provide a much deeper cancellation.

S21 mismatch over the frequency band of interest is essential in determining the cancellation bandwidth. Optics based approach is preferred compared with the electronics approach due to the much smaller fractional bandwidth and thus smaller S21 mismatch over the specific frequency band. Considering optics-based approaches, different S21 mismatches are seen. Figure 2.2 (a)-(b) show the S21 mismatch comparison over

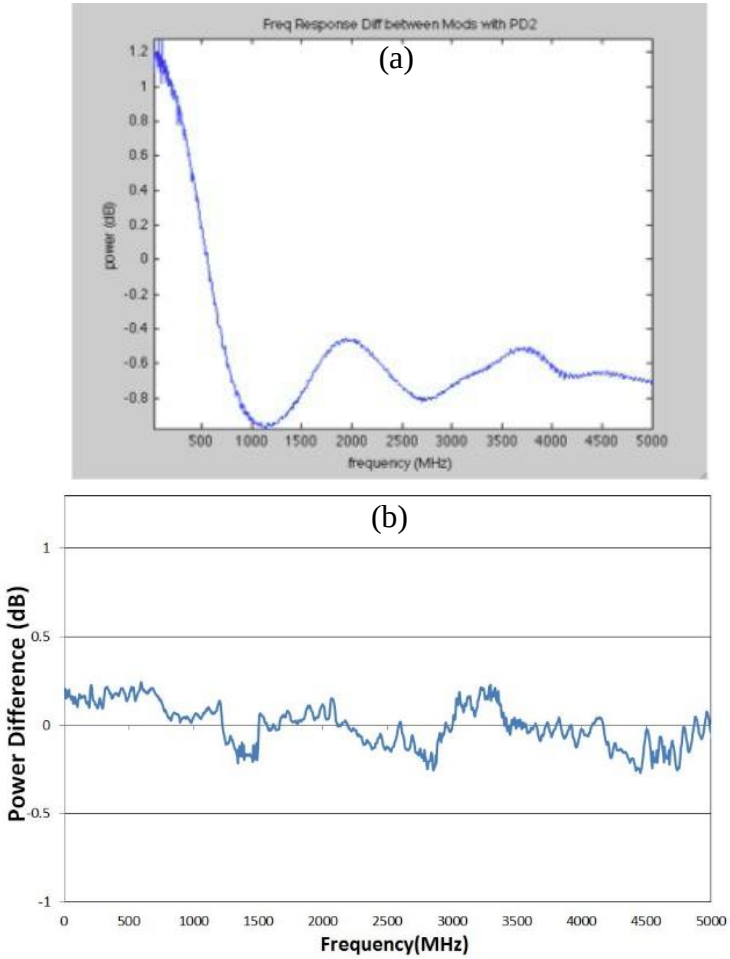

Figure 1.3. Comparison of S21 Mismatches over frequency between MZMs based approach and hybrid ICS.

frequencies between the MZMs based approach and the hybrid interference cancellation system (ICS). The hybrid ICS maintains a smaller S21 mismatch between two paths over a wide frequency range as shown in Figure 2.16, which explains the better cancellation bandwidth performance of the hybrid ICS over MZMs based approach.

CHAPTER 2

LINE OF SIGHT SELF-INTERFERENCE CANCELLATION SYSTEM

2.1 Introduction

Due to the proximity of the transmitter and receiver, the line of sight interference from the local transmitter is the strongest part of the co-site co-channel interference. In this chapter, we will focus on the interference cancellation of line of sight interfering signals.

As such, the following work is drawn and improved from an Optics Letters publication by Qi Zhou, Hanlin Feng, Guy Scott and Mable P. Fok entitled, "Wideband co-site interference cancellation based on hybrid electrical and optical techniques [12]," in which we present a hybrid interference cancellation system (hybrid ICS) that combines the advantages of both electrical and optical techniques. The hybrid ICS consists of electrical signal inversion in a RF Balun transformer, E-O conversion in electro-absorption modulated lasers (EMLs), as well as optically delaying and weighing the signal. The nearly ideal signal inversion obtained at the Balun transformer, the robustness and closely matched S21 response of the EMLs, and the high precision of the optical delay line and attenuator offer a promising solution to wideband co-site interference cancellation. We experimentally obtained ~35 dB of cancellation for 500-MHz bandwidth, >41 dB of cancellation for 100-MHz bandwidth, and >55 dB of cancellation for a 10-MHz bandwidth at various frequency bands. Cancellation performance of the hybrid ICS enables a weak

SOI that was completely masked by a strong broadband in-band interfering signal to be retrieved from the corrupted received signal.

2.2 Operational Principles

In a co-site interference scenario, the received signal r(t) consists of the weak SOI s(t) and a strong interfering signal i(t) that is from the adjacent transmitter and is coupled to the SOI at the receiver. Thus, the received signal is represented by $r(t) = s(t) + i(t)$.

Since the transmitter is co-located on the same structure in a co-site interference scenario, a copy of the interfering signal can be tapped from the transmitter, indicated as $i_0(t)$. In principle, the SOI s(t) can be retrieved from the received signal r(t) by subtracting $i_0(t)$ from r(t). However, due to channel effects when $i_0(t)$ propagates from the transmitter to the receiver, i(t) is no longer an identical copy of $i_0(t)$. Instead, the line-of-sight received signal i(t) is a delayed and attenuated copy of $i_0(t)$, as indicated as $i(t) = \alpha \cdot i_0(t + \tau)$.

Here, α represents the attenuation and τ is the time delay. Thus, to subtract the interfering signal from the received signal, attenuation and delay of $i_0(t)$ have to be precisely adjusted so that it emulates i(t).

Our proposed cancellation system is to subtract the known co-site interfering signal i(t) from the received signal r(t) such that the SOI s(t) is resulted. Since there is no subtraction in fiber optics, i.e. light is always a positive signal, subtraction is done by inverting the interfering signal $i_0(t)$ tapped from the transmitter, while delay and attenuation are precisely adjusted using an optical delay line and an optical attenuator. Figure 2.1 is the schematic illustration of our proposed hybrid interference cancellation system. The transmission

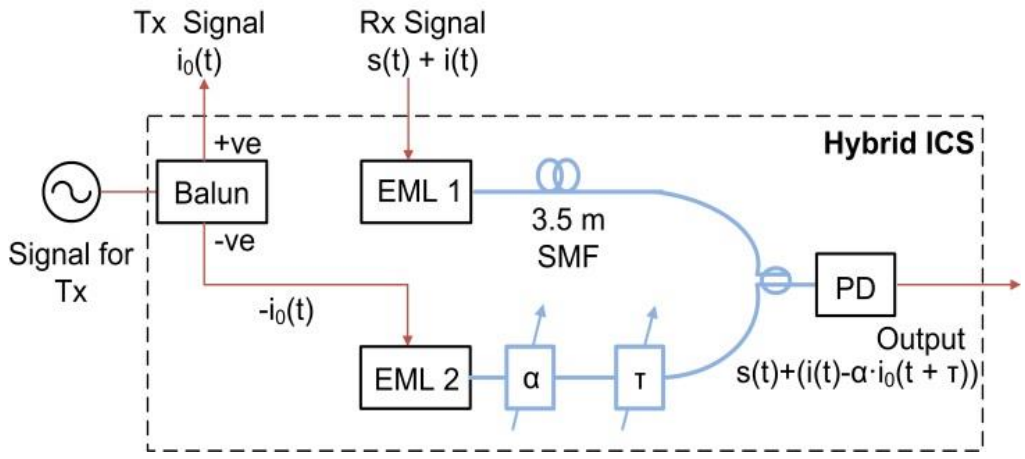

Figure 2.1. Schematic illustration of the hybrid ICS. Blue thick lines: Optical paths. Thin red lines: electrical paths. Tx: transmitter; Rx: receiver; RF balun transformer; EML 1-2: electro-absorption modulated lasers; α: tunable optical attenuator; τ: tunable optical delay line; SMF: standard single mode fiber; PD: photodetector.

signal is launched to a Balun such that two outputs, one with the same polarity as the input (positive output), and the other output with inverted polarity (negative output) are obtained. The positive output signal is used for transmission while the negative output is launched to the optical part of the hybrid ICS for cancellation. There are two EMLs in the hybrid ICS for converting signals from electrical domain to optical domain; one is for the received signal, and the another one is for the inverted interfering signal -- tapped negative output from the Balun. After the EMLs, both the received signal r(t) and tapped interfering signal $i_0(t)$ are now optical signals and propagate in the upper and lower branches of the hybrid ICS, respectively. Although the interfering signal $i_0(t)$ is tapped from the transmitter, it does not perfectly represents the interfering signal i(t) present in the received signal due to channel effects. While there are complex channel effects (multipath effects, dynamic channel response) during propagation, we focus on the static channel response for the line-of-sight signal in this paper. Multipath effects can be taken care of by modifying the hybrid

ICS into a multi-tap cancellation system [12], while the dynamic channel response can be compensated using adaptive filters [13]. When propagating from the transmitter to the receiver, the interfering signal is delayed and attenuated. Thus, the tapped negative output of the Balun is launched to a precise optical delay and an optical attenuator in the lower branch for processing. To match the amplitude and phase of i(t) with the tapped interfering signal $i_0(t)$, the optical delay and attenuator are adjusted such that maximum cancellation is obtained. The received signal from the upper branch and the matched inverted interfering signal from the lower branch are combined at the 3-dB optical coupler, such that $i_0(t)$ is subtracted from the received signal r(t), resulting in the desired SOI s(t). The resultant SOI is detected by a photodetector for converting it back into the electrical domain. The purity of the SOI as well as the strength of the residual interference after the hybrid ICS depends greatly on how closely matched the received interfering signal and the tapped interfering signal are, which depends on the precision of the optical delay line and optical attenuator, as well as the frequency response of the RF Balun.

2.3 Experimental Procedure and Results

We design a preliminary experiment to demonstrate the system's ability for canceling a simple sinusoidal signal efficiently. A signal generator with the output of 3 dBm and a frequency of 3 GHz is used to mimic the interfering signal. Figure 2.2 (a) and Figure 2.2 (b) demonstrate the results when the interference cancellation system is enabled and disabled, respectively. The ICS is finely tuned to cancel the interfering signal to below the noise floor. The cancellation is defined as the cancellation of the interfering signal provided

solely by enabling the ICS. It can be calculated through the difference in power of interfering signal before and after cancellation. In this preliminary experiment result, consider the maximum value (-19.82 dBm) minus the minimum value (-76.21 dBm) of interfering signal, a 57-dB cancellation is obtained for this single tone signal. A higher cancellation is possible when the noise floor is set to be lower.

(a) (b)

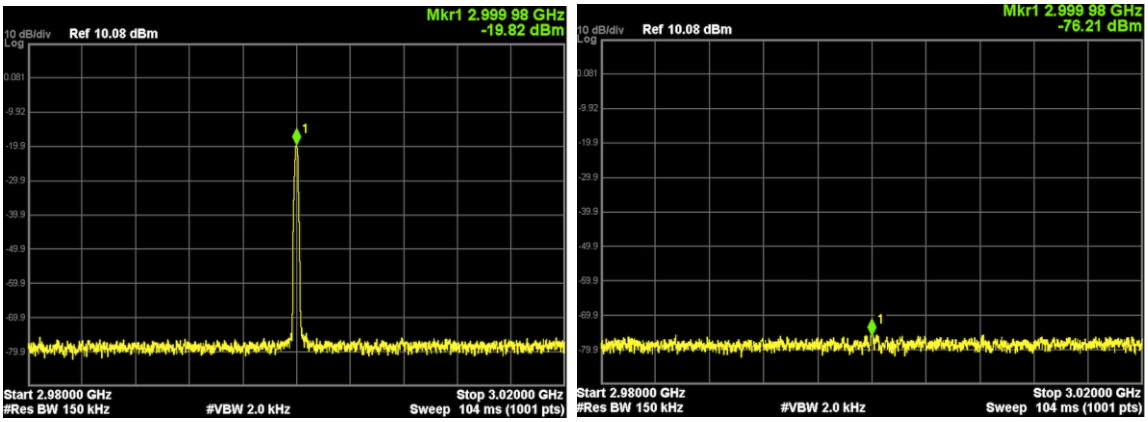

Figure 2.2. Cancellation of a single tone signal at 3 GHz as shown in the electrical spectrum analyzer (a) before cancellation (b) after cancellation spectrum.

Besides, we experimentally study the cancellation depth of our hybrid ICS at different frequency bands over various bandwidth of interest. A network analyzer is used to measure the S21 response of our hybrid ICS for determining the cancellation depth and cancellation bandwidth. The experimental setup is demonstrated in Figure 2.3. Wavelengths of the two EMLs are 1554.3 nm and 1553.7 nm, respectively and each EML has an output power of 1.82 dBm. The EMLs have a RF modulation bandwidth of 10 GHz. A precise tunable optical delay line with resolution of 0.03 ps is placed at the lower branch for delay/phase optimization, while a MEMS based optical attenuator controlled by a 16-bits digital-to-analog converter is used for matching the amplitude of the received interfering signal and the tapped interfering signal at the upper and lower branches in the hybrid ICS,

respectively. The insertion loss of the optical delay line and optical attenuator are 0.4 dB and 0.6 dB, respectively. The optical signal from the upper and lower branches are combined at the 3-dB optical coupler and detected by an 18 GHz photodetector (Discovery Semiconductor DSC-R401HG). To determine the amount of cancellation, the hybrid ICS is first disabled by disconnecting the lower branch of the system, such that the measured S21 response represents the interfering signal level from the received signal before cancellation, indicated as $S21_{before}$. Then, the lower branch of the system is reconnected to enable the hybrid ICS, while the delay and attenuation are optimized to obtain the best cancellation results. With the hybrid ICS enabled, the S21 response represents the interfering signal after cancellation, indicated as S21after. By taking the difference between S21before and S21after measured in dB, the amount of cancellation is determined.

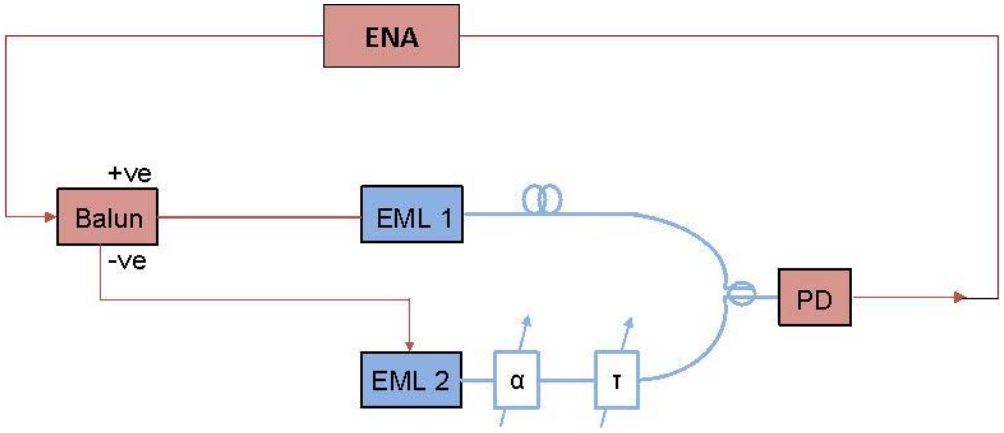

Figure 2.3. Experimental setup for cancellation performance measurement. Blue thick lines: Optical paths. Thin red lines: electrical paths. ENA: electrical network analyzer; Balun: RF balun transformer; EML 1-2: electro-absorption modulated lasers; α: tunable optical attenuator; τ: tunable optical delay line; PD: photodetector.

Our system demonstrates an impressive 50-dB cancellation depth over 150 MHz at 900 MHz band as shown in Figure 2.4 (a). Figure 2.4 (b) - (d) illustrate the measured cancellation over 400-MHz bandwidth achieved by the hybrid ICS with a center frequency at 900 MHz, 1.5 GHz and 2.4 GHz respectively. 400-MHz bandwidth is picked because most of current applications do not have a wider bandwidth. The results shown in Figure 2.6 indicate a >36-dB cancellation over 400-MHz bandwidth at the 900 MHz band, a >37-dB cancellation over 400-MHz bandwidth at the 1.5 GHz band and >33-dB cancellation over 400-MHz bandwidth at the 2.4 GHz band, respectively. The setting of the hybrid ICS is adjusted to obtain the best cancellation over the whole 400-MHz bandwidth. As shown in both Figure 2.4 (b) - (d), cancellation is enhanced when the bandwidth of interest is decreased. The Figure 2.4 (b) – (d) indicate a bandwidth of 220-MHz for 900 MHz band, 400 MHz for 1.5 GHz band and 310-MHz for 2.4 GHz band, and the corresponding cancellation are 45 dB, 37 dB and 40 dB, respectively. Moreover, a 5.5-GHz ultra-wideband cancellation bandwidth is achieved with over 30-dB cancellation, as shown in Figure 2.4 (e). To the best of our knowledge, this is the first demonstration of such a wideband interference cancellation. This capability enables simultaneous cancellation of multiple interfering signals at various frequency bands.

We have measured the cancellation performance of the hybrid ICS at different bandwidths and frequency bands, the results are summarized in Table 2.1. It is worth noticing that our hybrid ICS works well for a wide range of frequency and bandwidth, with only minor delay and attenuation adjustment needed. The difference in cancellation depth at different frequency band is mainly due to the difference in frequency response of the two Balun outputs, RF cables, and EMLs in the upper and lower branches.

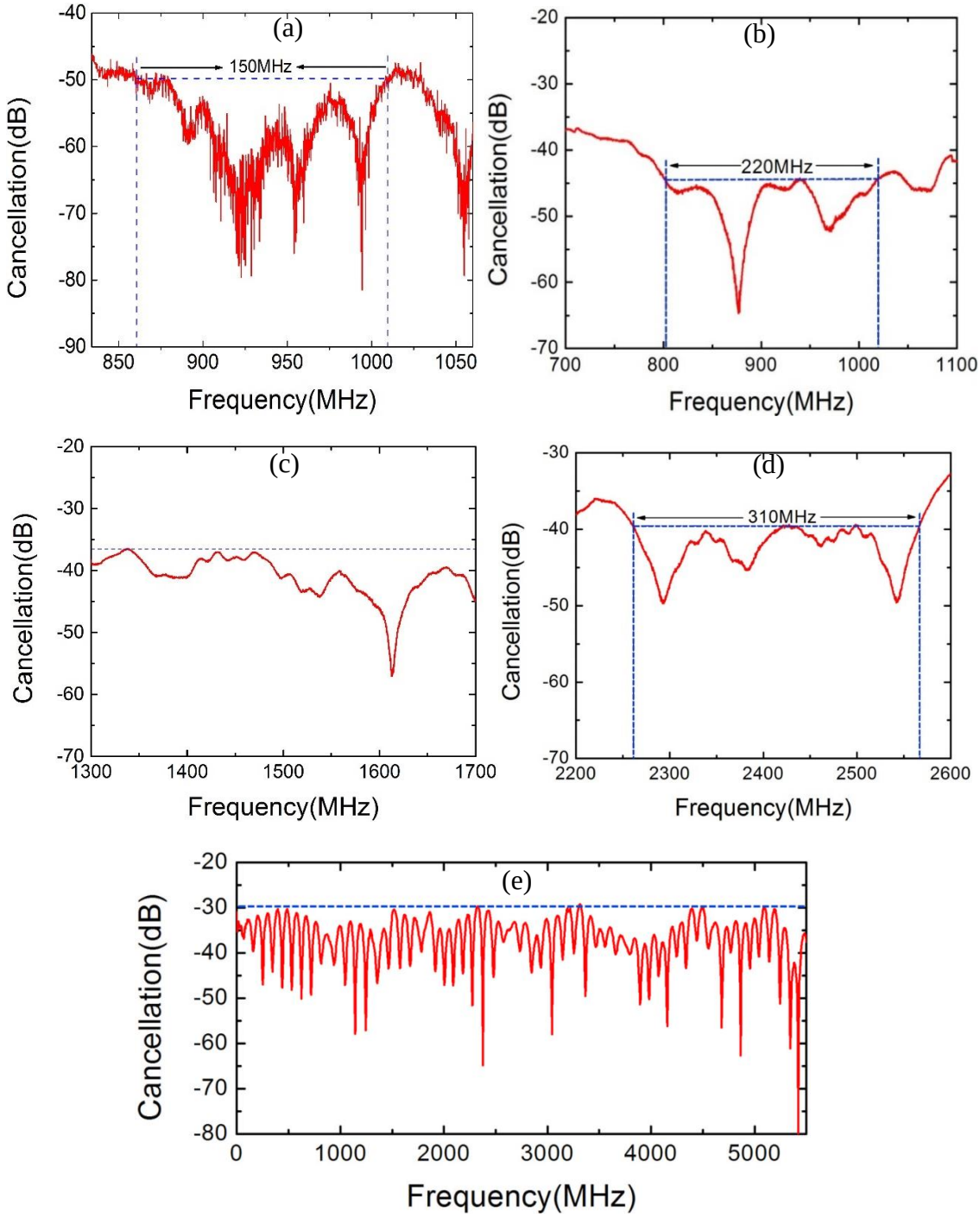

Figure 2.4. Measured cancellation performance of hybrid ICS (a) with 250-MHz (b) with 400-MHz bandwidth at 900 MHz band, (c) with 400-MHz bandwidth at 1.5 GHz band, (d) with 400-MHz bandwidth at 2.4 GHz band, (c) 5.5-GHz bandwidth.

Table 2.1. Cancellation bandwidth and cancellation depth (in dB) at various frequency bands.

	Bandwidth (MHz)				
Center Frequency (MHz)	10	50	100	200	500
500	56.9	48.2	46.7	32.6	31.3
700	56.1	44.2	43.2	39.3	38.1
800	56.7	48.6	45.4	37.5	37.3
900	57.5	49.5	44.8	44.6	36.5
1500	56.2	44.7	41.6	37.3	37.0
2400	57.4	46.7	41.8	40.0	33.0
4900	50.4	44.3	43.4	43.2	37.2

In a co-site interference scenario, the weak SOI is masked by a strong interfering signal. For cancelling out interfering signal from the received signal and recovering the weak SOI, a weak SOI that is ~15 dB above the noise floor and a strong interfering signal that is >25 dB stronger than the weak SOI are used. The SOI and interfering signal are generated separately using two individual signal generators. The SOI is a single tone signal while the in-band interfering signal has a bandwidth of 400-MHz. They are coupled together to mimic the received signal.

Figure 2.5 (a) - (c) show the performance of the hybrid ICS in recovering a weak SOI from the frequency spectrum under a strong interfering signal at the 900 MHz, 1.5 GHz and the 2.4 GHz frequency bands, respectively. An RF spectrum analyzer is used to for measurement. The red curve in Figure 2.7 is the measured received signal that consists of both the strong interfering signal and the weak SOI. As shown, the weak SOI is completely buried by the in-band interfering signal and it is impossible to identify the frequency or even the presence of the SOI, i.e. even filtering will not work to isolate the SOI from the

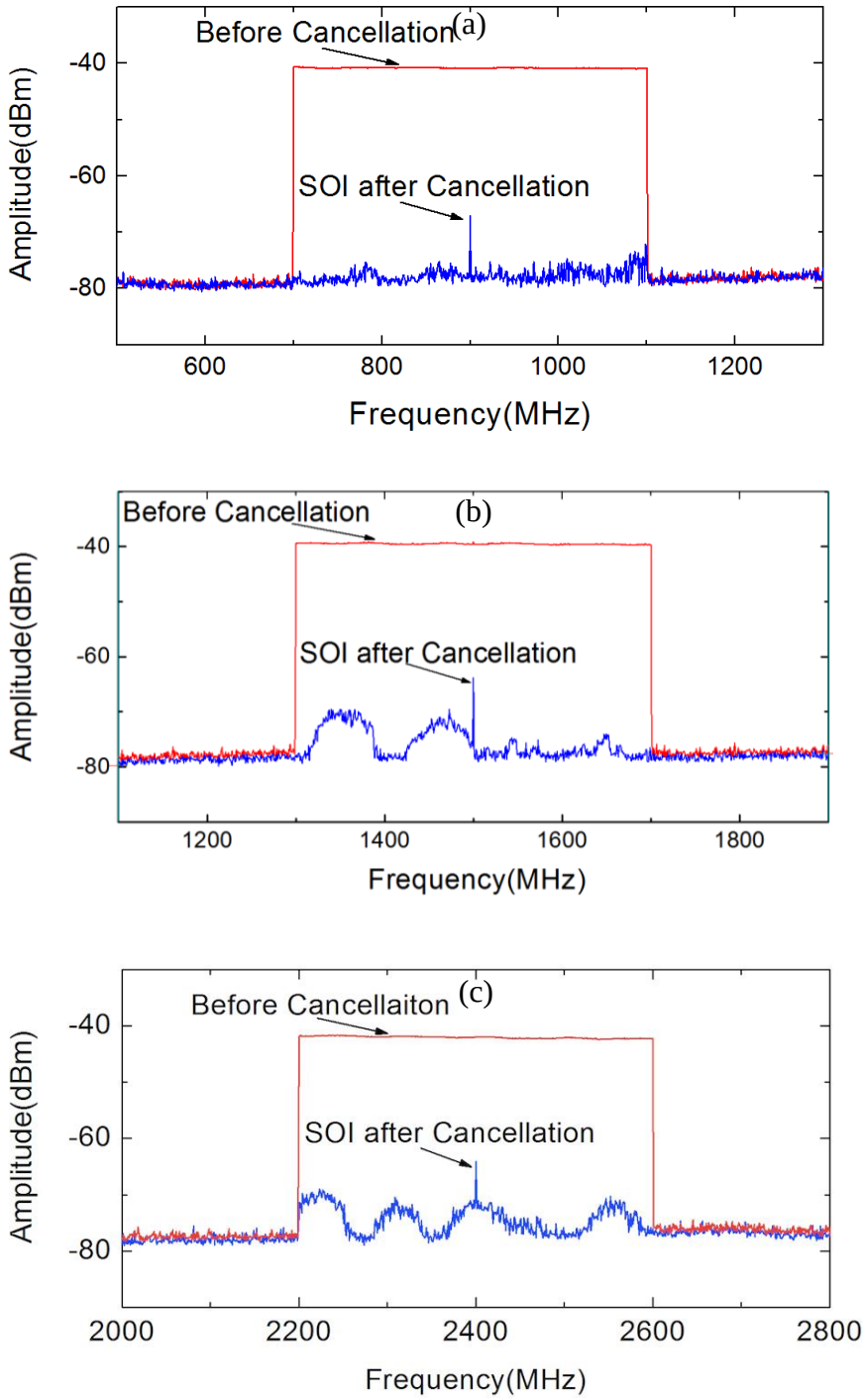

Figure 2.5. Measured RF spectra of the received signal before interference cancellation (red curve) and after interference cancellation with hybrid ICS (blue curve). (a) at 900 MHz band (b) at 1.5 GHz band. (c) at 2.4 GHz band. SOI: signal of interest.

interfering signal. To cancel out the 400-MHz strong interfering signal, the hybrid ICS is enabled and the optical delay and attenuation is tuned such that the residual interfering signal is minimum at the output of the hybrid ICS, the resultant signal after cancellation is shown by the blue curves in Figure 2.5 (a) - (c) for 900 MHz and 2.4 GHz bands, respectively. The SOI is now recovered from the received signal and is clearly shown in the resultant RF spectra.

Now, the SOI is visible in the RF spectrum and RF filters can be used to further remove the out of band interfering signal if needed. The above experimental results successfully demonstrate the ability of the hybrid ICS to recover the weak SOI from a received signal that consists of a strong in-band interfering signal in a co-site interference scenario.

We have characterized the effect of interfering signal onto the signal of interest as well as the performance of the hybrid ICS through eye diagram and bit-error rate measurements. A strong sweeping RF source from 3.5 GHz to 6.5 GHz is used as the in-band interfering signal, while a 10-Gbit/s PRBS signal is used as the SOI. Figure 2.6 (a) and (b) show the eye diagrams before and after enabling our hybrid ICS, respectively. The eye diagram is completely closed and a BER of 0.736×10^{-1} is resulted due to the presence of the strong interfering signal. After enabling our hybrid ICS, a widely opened eye diagram as well as error free performance is obtained. To test the system's performance for lower data rate, a 200-Mbit/s PRBS signal is used as the SOI. Under the interference from a strong 200-MHz transmitting (interfering) signal, the eye diagram is completely closed, as shown in Figure 2.6 (c). With the use of the hybrid ICS, a widely opened eye diagram of the SOI is recovered (Figure 2.6 (d)).

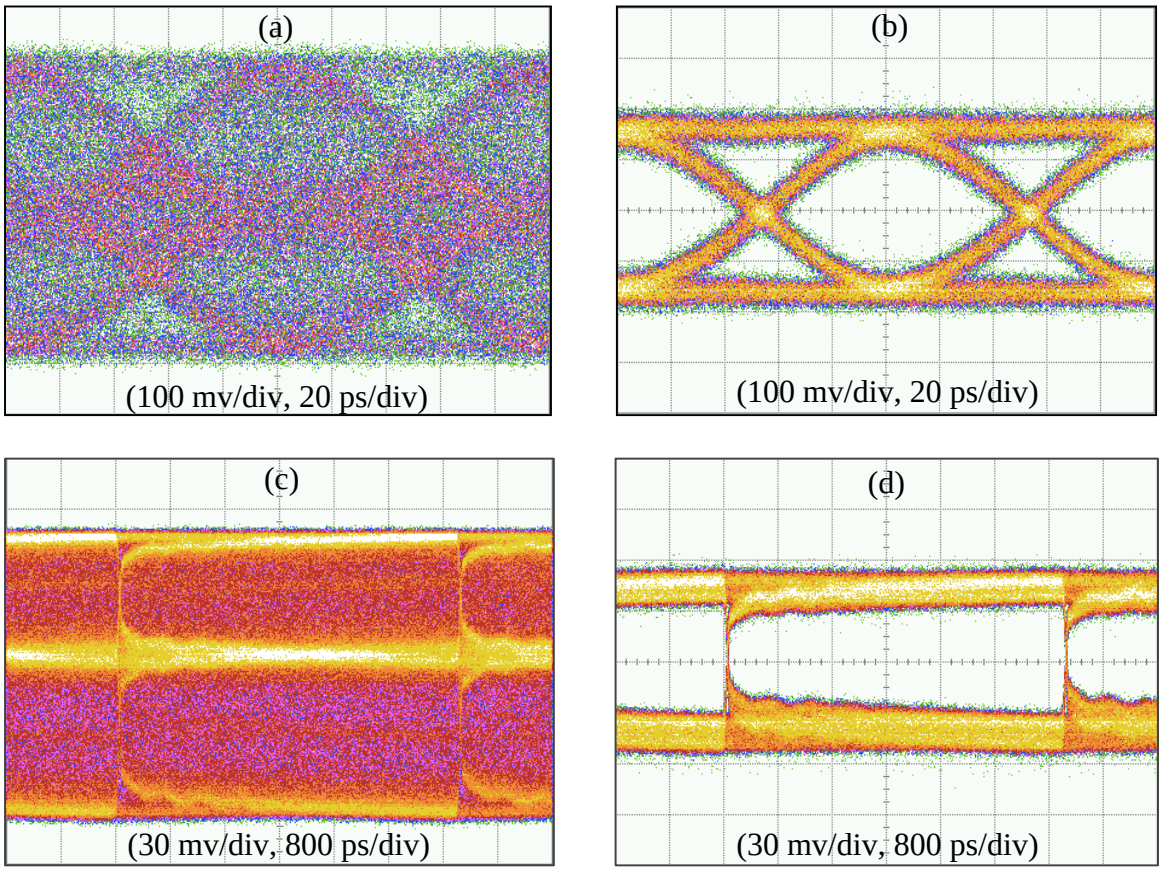

Figure 2.6. 10 Gb/s Eye diagrams (a) before and (b) after cancellation; 200 Mb/s Eye diagrams (c) before and (d) after cancellation.

The hybrid ICS has a good linearity, which is verified through a two-tone spurious free dynamic range (SFDR) measurement. The two-tone signals at 890 MHz and 910 MHz are combined before modulating the EML1. By finding the intercept point after doing the linear match for both fundamental product and intermodulation product as shown in Figure 2.7, third order intercept point (IIP_3) is calculated to be 21.9 dBm. The measured noise floor is -118 dBm/Hz. With pre- and post-amplification, a link loss of 1.2 dB is obtained in our system. As a result, a SFDR of 93.2 $dBm/Hz^{2/3}$ is obtained.

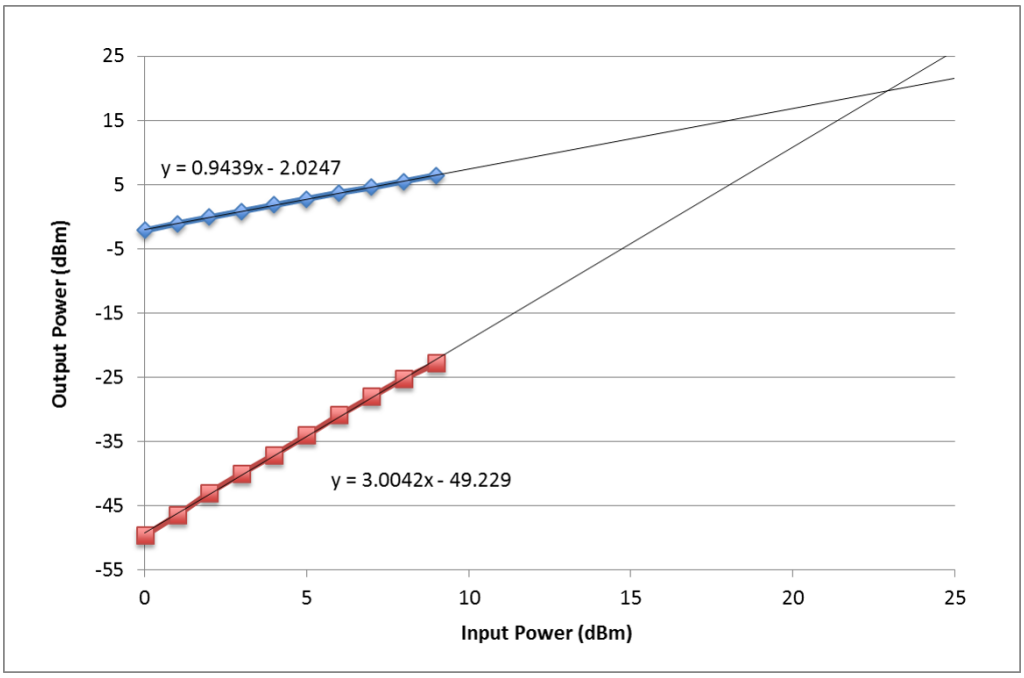

Figure 2.7. Transfer function (fundamental product, blue line) and intermodulation functions (intermodulation product, red line) for the hybrid interference cancellation system.

2.4 Summary

We have proposed and experimentally demonstrated a wideband co-site interference cancellation system for RF signal based on hybrid optical and electrical techniques. The hybrid ICS consists of an RF Balun for signal phase inversion, EMLs for E-O conversion, while tunable optical delay line and tunable optical attenuator are used to provide precise amplitude and phase matching to channel effects. The proposed ICS takes advantages of the excellent frequency response of the Balun and EMLs, as well as the high precision tuning offered by the optical delay line and attenuator. We experimentally obtained 30-dB cancellation over an extremely wide bandwidth of 5.5 GHz. Good cancellation

performances are obtained at various center frequency bands from 500 MHz to 4900 MHz. The recovery of weak SOI that was masked by a strong wideband interfering signal is experimentally achieved. A widely open eye diagram and error free BER performance are obtained for a 10-Gb/s signal of interest with the use of the hybrid ICS for removing a wideband sweeping interfering signal.

2.5 Video Transmission based on Hybrid ICS

In previous sections, we developed the hybrid interference cancellation system (ICS) using electrical and optical components, which achieve decent cancellation for transmitting and receiving signals simultaneously with the same frequency band. In this section, we apply the hybrid interference cancellation system in a video transmission system, to investigate the hybrid ICS system towards a real video signal.

There are a lot of applications of this system including military operations where there are often many communication systems carried on one vehicle constantly in use where privacy and precision are vital. Specific video applications could be a military medical transport situation where a surgeon or emergency medical technician (EMT) on the vehicle might transmit high quality video to other doctors off-site for their input and assistance, while the vehicle is also receiving video of interest in their area. In this scenario, two different video signals, both operating on the same frequency band are creating co-site co-channel interference, the medical video is interfering with the video that the vehicle wants to receive. The proposed hybrid ICS system is able to cancel the co-site interference and give the receiving video clarity needed in this critical situation.

Another scenario and application for the hybrid ICS is on bomb-disposal robots. These robots are usually operated remotely by sending video to the operator at a safe distance. In general, improvised explosive devices (IED) are operated remotely by simple remote control devices like cell phones. To disable the remote communication for control on the IED, the bomb robot will generate a strong jamming signal. But with the large jamming signal, the electronics on the robot are not sophisticated enough to send video back to the operator and receive commands in the presence of the strong co-site co-channel interference.

In both of the above cases, sending and receiving signals simultaneously at the same station creates co-site interference. The receiving antenna will receive a very strong interfering signal from the local transmitter due to proximity. However, the vehicle is interested in receiving a signal from a far-away source, base camp, satellite, etc., but the interfering signal overwhelms the much weaker signal of interest. Due to the limited availability of frequency spectra, both the transmitting and receiving could be of the same frequency band, creating co-site co-channel interference. In this section, we will show how

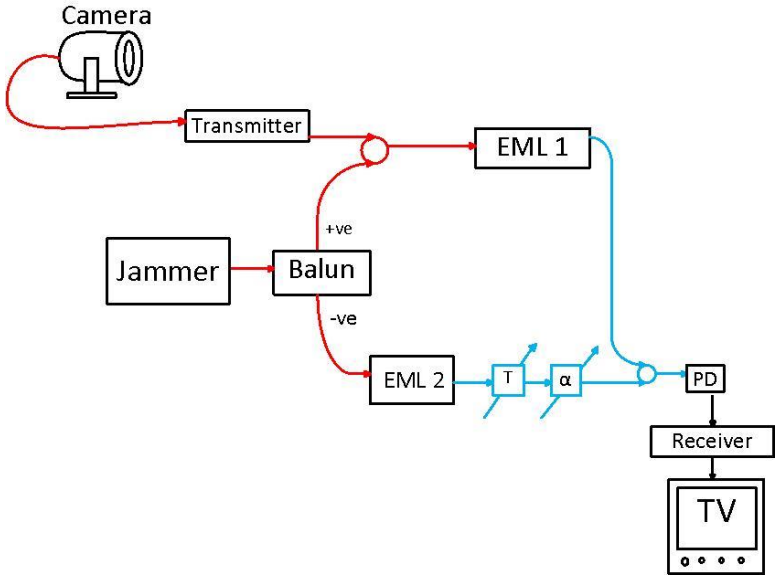

Figure 2.8. Experimental setup for the video transmission.

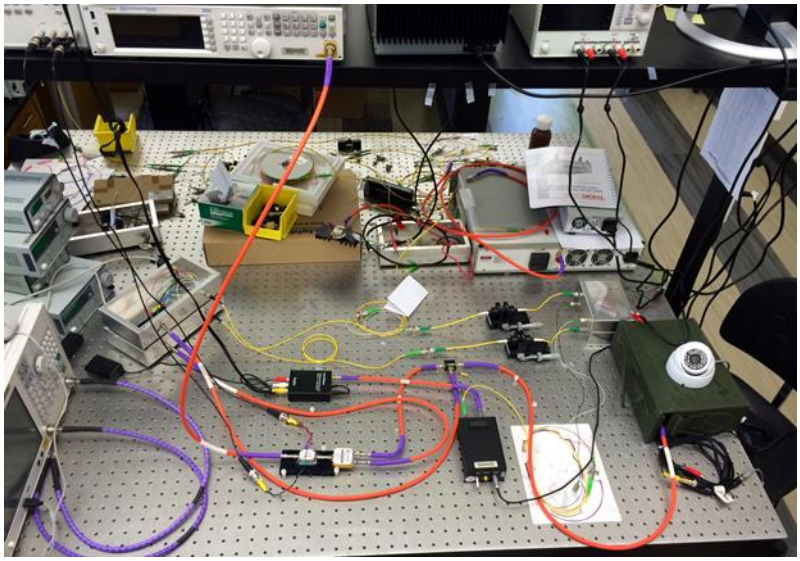

Figure 2.9. Actual experimental setup.

the hybrid ICS can efficiently cancel out the strong interfering signal. Figure 2.8 shows the experimental setup. A CCTV camera is connected to the transmitter, while the transmitter is housed in the ammunition box to reduce wireless transmission of the signal, therefore bypassing the addition of the extra signal of interest. A strong broadband jammer is generated through the amplification and filtering of the ASE noise from the EDFA. The Balun is used to split and generate the inverted copy of the jammer with its positive output interferes with the video signal and both of the outputs modulate the two EMLs. The attenuator and delay are incorporated to mimic the channel response of the jammer transmission path. After converting back to the electrical domain by the photodetector, a TV is connected after the receiver to monitor the video signal. The actual experimental setup is shown in Figure 2.9.

The 3-dB bandwidth of the video signal spectrum is around 10 MHz, as shown in Figure 2.10 (a). The measurement is taken with 30 dB of attenuation on the transmitter. The transmitter has a power of 1W, so the 30 dB attenuator is attached to the transmitter for the duration of the testing. The attenuated output is used as the signal of interest. Figures 2.10

(b) shows the cancellation performance of the ICS over 400 MHz at the 2.4 GHz band, which is much better than traditional electrical based ICS systems. Before enabling the ICS, the TV cannot detect the video signal from the receiver because the presence of the strong in-band jammer as shown in Figure 2.11 (a). However, after enabling the ICS, the video signal taken by the camera is fully recovered and clearly displays on the TV as shown in Figure 2.11 (b).

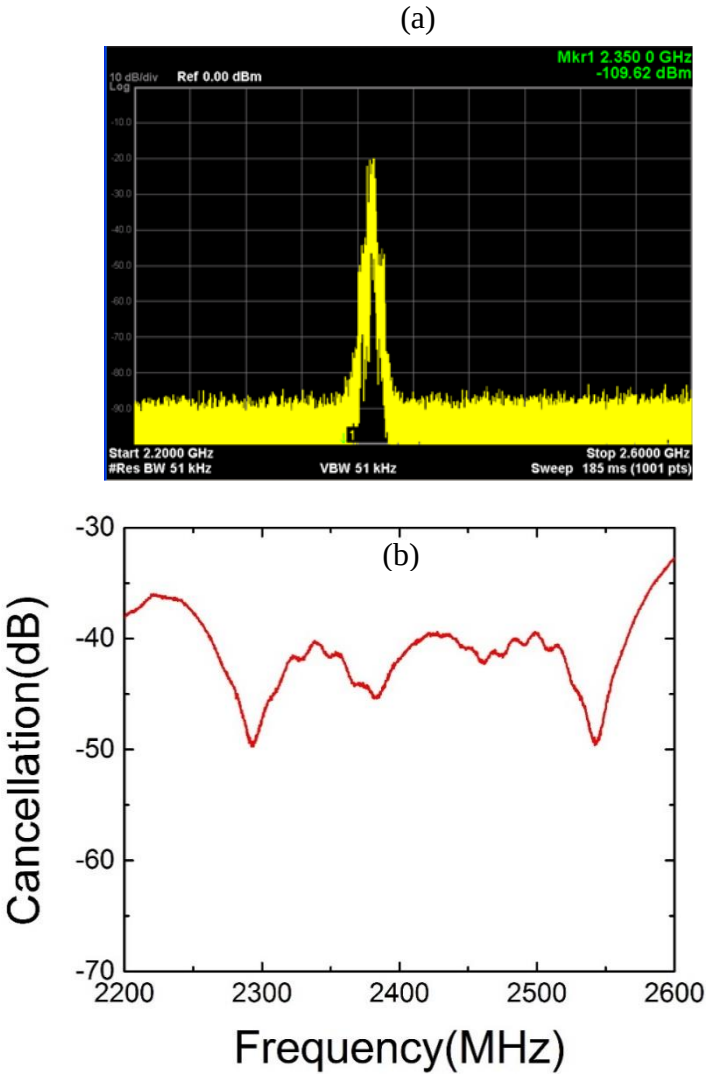

Figure 2.10. (a) Measured electrical spectrum of the video signal; (b) cancellation performance of ICS at interesting band.

(a)

(b)

Figure 2.11. Monitored video signal on TV (a) before (b) after enabling the ICS.

2.6 Wireless Stealth Transmission

Due to the high performance of the hybrid ICS, its application can be further extend beyond interference cancellation. In this section, we explore its application in providing enhanced security for wireless communications. Due to the broadcasting and wireless nature of wireless system, the physical layer of a wireless system is vulnerable to a variety of attacks, including jamming, eavesdropping, and interception [14]. Adversary can easily tap into a communication channel, obtain information, or alter information in the communication channel. Securing information in the transport layer becomes challenging due to the massive amount of data required to be processed as well as the limited computational power. Thus, enhancing security in the physical layer become attractive due to the fact that the bottleneck in computation power can be eliminated. Stealth transmission is a promising way to enhance security on top of other security measures because no sign of signal transmission can be found in a stealth transmission. Thus, the adversary will not be looking for the sensitive signal. Stealth transmission in radio frequency is not trivial because of the increasing bit-rate and bandwidth that reaches the limitation of high-speed electronics.

Spread spectrum is one of the example for radio frequency stealth transmission, 1 Mbps spread spectrum communication for stealth transmission has been demonstrated [15]. Photonic techniques have shown its applications in Radio frequency signal processing due to its unique broadband, low loss, high frequency, and electro-magnetic immunity properties. In the former sections, we develop a photonic-based radio frequency interference cancellation system (ICS) that is capable of cancelling wideband co-site co-channel interference in wireless system. We experimentally obtain 30 dB and 50 dB of

cancellation over a bandwidth of 5.5 GHz and 150 MHz, respectively as discussed in the former section. In this session, we utilize this high performance ICS for removing the public signal from the public channel for stealth transmission. The ICS inverts a copy of the public signal and "subtract" it from the received signal. The ICS provides a good cancellation performance so that the strong public signal is greatly suppressed and the weak stealth signal is recovered. The proposed scheme works well for high-speed baseband and carrier modulated stealth transmission.

Principle and experimental setup

The experimental setup of the photonic ICS for stealth transmission is shown in Figure 2.12. To better understand how the ICS based stealth transmission work, we will explain the working principles. The ICS is shown in the blue shaded dashed box on the right in Figure. 2.12, where R(t) is the received signal at the antenna. At the base station, P(t) is the public channel and S(t) is the stealth signal that we would like to recover. The received

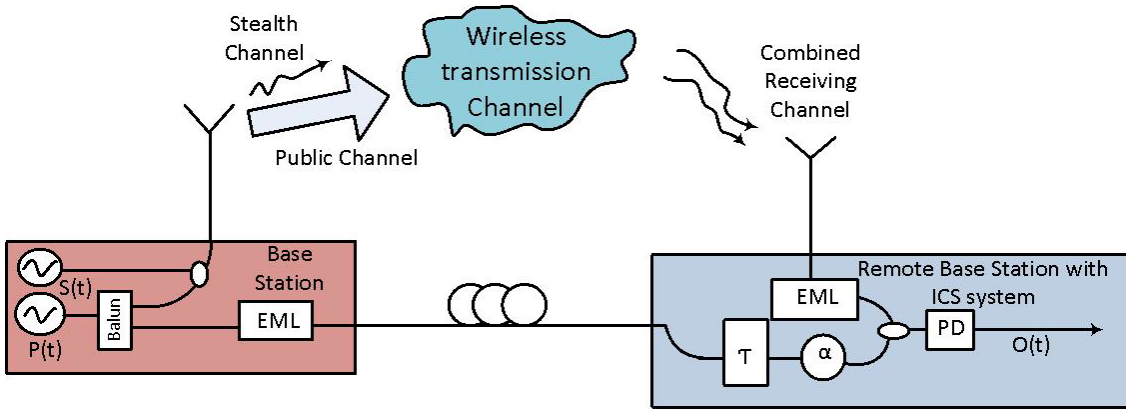

Figure 2.12. Schematic setup for the stealth transmission based on ICS. Balun: RF balun transformer; EML 1-2: electro-absorption modulated lasers; α: tunable optical attenuator; τ: tunable optical delay line; PD: photodetector.

signal R(t) at the remote base station consists of a delayed and attenuated version of the public channel P'(t) as well as the stealth signal S(t).

Basically, what the ICS is performing is a subtraction operation between the received signal R(t) and the public channel P(t), such that the output of the ICS is O(t) = R(t) – P(t). With precise adjustment of P(t), the same delay and power of the P'(t) can be obtained, such that O(t) = P'(t) + S(t) – P'(t), resulting in O(t) = S(t), which is the stealth channel alone. Although the operation involves a simple subtraction operation, the precision required for time delay and attenuation over frequency is high. Therefore, it is challenging to obtain both amplitude and phase matching over a wide range of frequencies between the receiving branch and the cancellation branch for in order to achieve high cancellation depth over a wide bandwidth.

The scenario for radio frequency (RF) stealth transmission is shown in Figure 2.14 and is described as follow. First, both the stealth signal and public signal are generated at the base station, and they are combined and transmitted through the public channel, while a portion of the public signal is tapped and launched to the balun where an inverted copy of the public signal is obtained. The inverted public signal is modulated onto an external modulated laser (EML1), and is transmitted through an optical fiber to the remote base station. The fiber optic links that is commonly found in wireless base station to implement Fiber-To-The-Antenna (FTTA) can be used. The fiber optics link for FTTA was designed to reduce losses and make it easier to connect multiple antenna sites to a common base station processing unit. At the remote station, the public signal is then subtracted from the received signal using the photonic ICS such that the stealth signal can be recovered.

Experimental results and discussion

In our experiment, a 150 Mbps PRBS signal is used as the public signal, while another 150 Mbps PRBS signal is used as the stealth signal. The positive copy of the public signal is combined with the stealth signal, which is 35 dB weaker in power for transmission. The power of the stealth channel has to be significantly lower than the public channel such that it is invisible in both the temporal and spectral domain. System noise can further mask the stealth signal. The combined public signal and stealth signal are used for transmission. Figure 2.13 (a) and 2.13 (b) show the eye diagrams of the public signal alone and the public signal with stealth signal, respectively. As shown from the eye diagrams, it is hard to find any difference between the public signal with and without stealth signal in temporal domain. To ensure secure stealth transmission, we have to ensure that the stealth signal is also hidden in spectral domain. The RF spectra are measured as shown in Figure 2.14 (a)-(c), corresponding to spectra of public signal only, public signal with stealth signal, and stealth signal only, respectively. From both the temporal and spectral domains, it is shown that the stealth signal is hidden in the public channel and stealth transmission is successfully achieved.

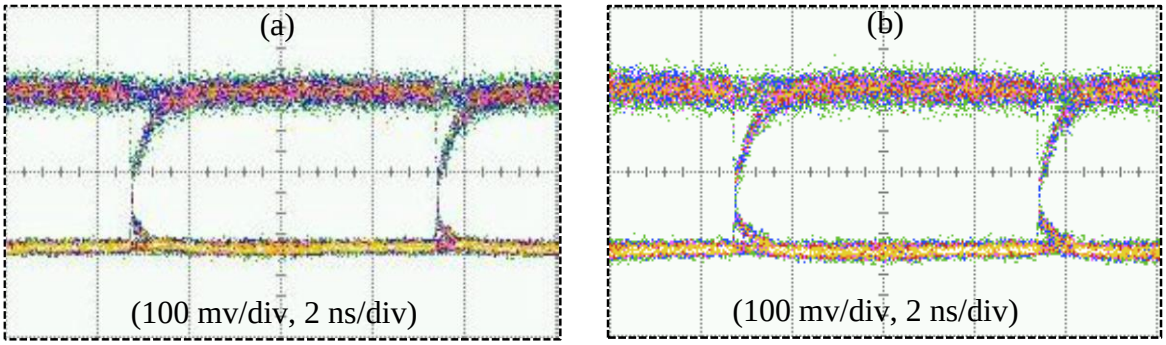

Figure 2.13. (a) Eye diagram of public signal only; (b) Eye diagram of public signal with stealth signal.

At the receiver side, the combined received signal is modulated onto an optical carrier through another external modulated laser EML2, to convert it to optical domain for processing. Since there is no subtraction in optical signal (i.e. optical signal is always positive), the negative copy of the public signal transmitted through an optical fiber is used for "subtraction" when it is combined with the received signal optically at the optical coupler. Tunable optical delay line and variable optical attenuator are used for adjusting time delay and power of the negative copy of the public signal, such that it is aligned with the received public signal at the proper power level. Both the combined received signal branch and the inverted public signal branch of the ICS are combined with an optical

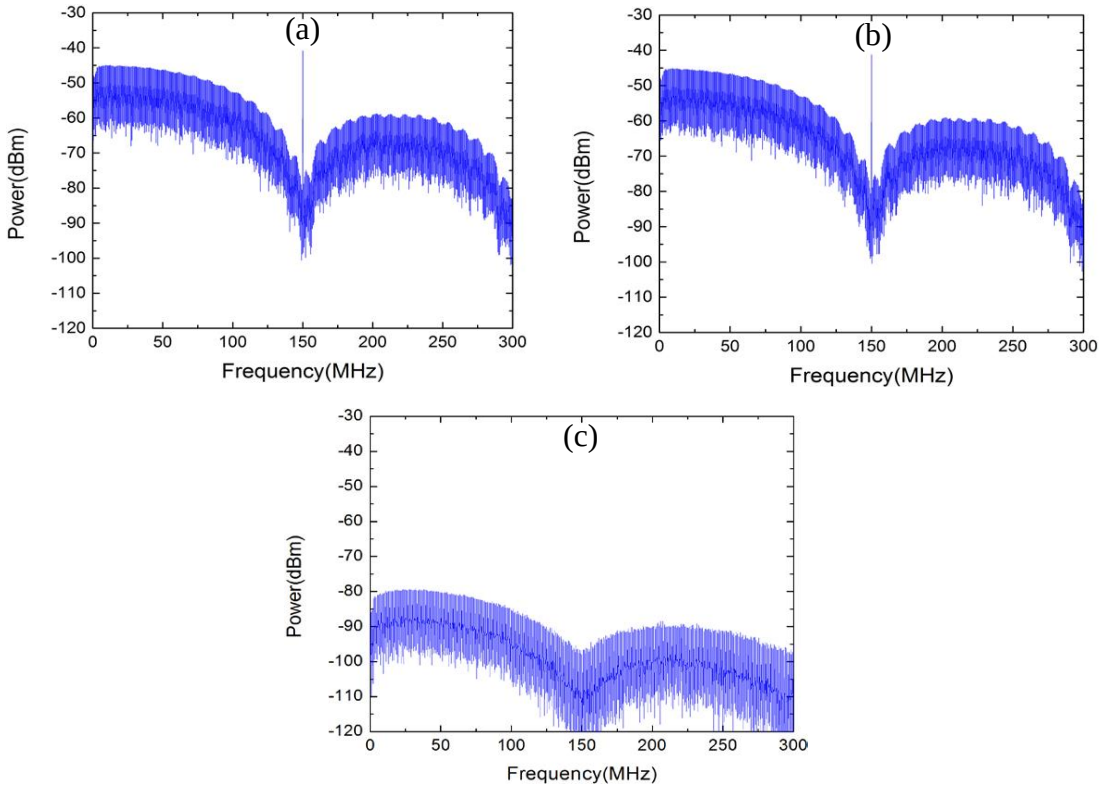

Figure 2.14. RF spectrum of (a) public signal only; (b) public signal with stealth signal; (c) stealth signal only.

coupler such that the public channel can be “subtracted” from the received signal. At the output of the ICS, a recovered stealth signal is obtained and is detected by a photodetector. Due to the wide operation bandwidth of the photonic ICS, the proposed stealth transmission works well for both baseband communications and carrier modulated communications. The wide operation bandwidth of the photonic ICS is acquired as the result of the good S21 matching of the balun and EMLs, and the high precision of the tunable optical delay line and variable optical attenuator. The ICS has a deep cancellation of 30 dB over a 5.5GHz bandwidth, which essentially covers most of the commonly used wireless communication systems. An improved cancellation depth is obtained when focusing on a relatively narrower bandwidth of 150MHz, for which a 50-dB cancellation is obtained. With the ICS, the public signal is greatly suppressed and the stealth signal is able to be recovered. The performance of ICS is sensitive to the delay and attenuation precision. Without a correct delay and power setting, the stealth signal cannot be recovered. Showing in Figure. 2.15 are the RF spectra with and without enabling the ICS, the S21 amplitude and phase

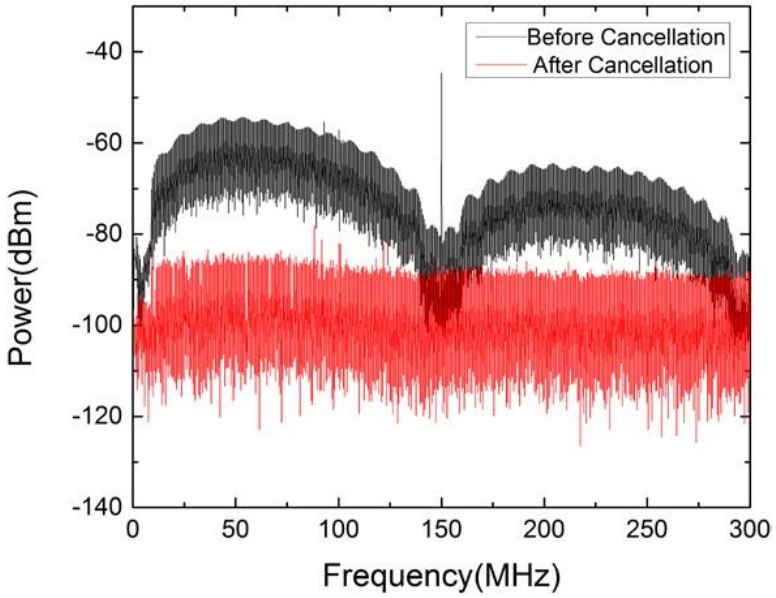

Figure 2.15. Measured RF spectra before (black curve) and after cancellation.

response are not perfectly matched in this setting, resulting in less cancellation of the public signal as expected. Thus, the precision of the delay and attenuator settings also provides another degree of security to the system. The measurement of RF spectrum after cancellation is not clear enough because it's close to noise floor. This can be improved with a better resolution bandwidth.

Summary

We propose and experimentally demonstrate stealth transmission for radio frequency wireless systems based on a photonic interference cancellation system. The ICS makes use of the well-matched phase and amplitude response of the balun and EMLs, together with the high precision provided by the tunable optical delay line and variable optical attenuator to achieve a deep cancellation over a wide bandwidth. Due to the broadband operation of the ICS, the proposed scheme works well for high-speed stealth signal transmission.

CHAPTER 3

MULTIPATH INTERFERENCE CANCELLATION

3.1 Introduction

In the former chapters, we've utilized the hybrid interference cancellation system to deal with radio frequency signal cancellation over a wide range of frequency band. Our system is capable of cancelling out unwanted, co-site co-channel microwave signals using the broadband characteristics of fiber optics. 50-dB cancellation over 150 MHz and 30 dB cancellation over an ultra-wide bandwidth of 5.5 GHz have been obtained. To enhance our proposed system for fitting better with the real applications. Multipath interferences have to be taken into account as multipath effects are unavoidable in wireless communications as shown in Figure 3.1. In actual scenarios, the interfering signal will propagate through different paths due to reflection and diffraction because of the complex channel

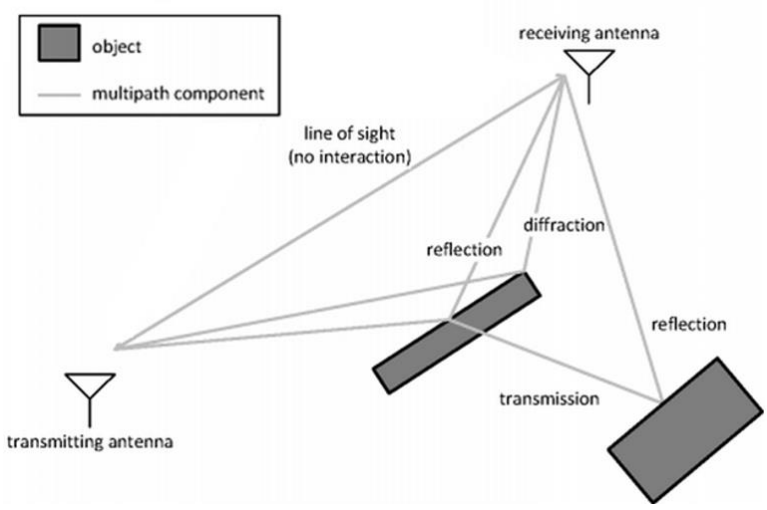

Figure 3.1. Illustration of multipath effect.

"http://www.wica.intec.ugent.be/research/propagation/physical-radio-channel-models"

environment. Multiple interferers with different delays and attenuations will be received simultaneously at the receiver. The rake receiver is widely used for mitigating multipath interference, which incorporates correlators to estimate and compensate each path of wireless channel. Besides, several electrical based multipath interference cancellation structures have been proposed recently [16]-[18]. In these approaches, channel estimation is performed first, after that the replica of multipath interference is duplicated and removed from the received signal, with only the desired signal reserved. Nevertheless, the electrical based approaches suffer from the inherent bandwidth limitations of electrical devices.

An analog optical technique for multipath interference cancellation was proposed recently based on counter biasing MZMs and multiple optical delay lines and attenuators [12]. While a broader cancellation bandwidth over electrical based approaches obtained, their performance is still limited by the S21 mismatch between the two MZMs during electrical to optical conversion.

Our approach evolves from the line of sight scheme described in section 2.2. Multiple delay lines and attenuators have been incorporated to compensate the multipath channel effects. Our scheme is able to support self-interference cancellation for up to third order of multipath components, while decent cancellation performance is demonstrated at different frequency bands of interest.

3.2 Working Principles

Figure 3.2 is the experimental setup of the multipath self-interference cancellation system. The local transmitting signal is propagating through both the line of sight and the multipath.

At the receiver end, the resultant interfering signal i(t) is consist of the summation of multipath components (delayed and attenuated copies) of the original transmitting signal $i_0(t)$.

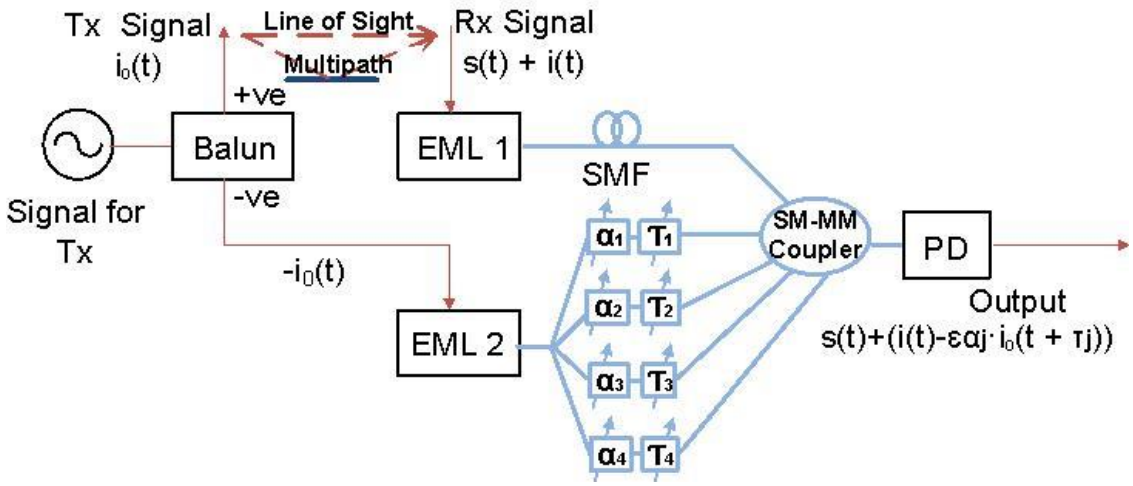

Figure 3.2. Schematic illustration of the multipath hybrid ICS. Blue thick lines: Optical paths. Thin red lines: electrical paths. Tx: transmitter; Rx: receiver; RF balun transformer; EML 1-2: electro-absorption modulated lasers; α_j: tunable optical attenuators; τ_j: tunable optical delay lines; SMF: standard single mode fiber; SM-MM: single mode to multi-mode coupler; PD: photodetector.

The theory is similar to the system discussed in chapter 2. The Balun transformer provides nearly ideal signal inversion, while the two EMLs have been used to modulate the signals into the optical domain that offer a closely matched S21 response. Multiple delay lines and attenuators indicated as τ_j and α_j are set up to provide precise channel compensation for multipath effects. The cancellation performance of this multipath self-interference cancellation system enables the weak SOI masked by the strong broadband in-band interfering signal to be recovered from the received signal. The recovery of a weak

Phase-shift keying (PSK) signal of interest from a strong PSK interfering signal has been studied to investigate the modulation dependency of the hybrid ICS.

Since the interfering signal is delayed and attenuated when propagating from the local transmitter to local receiver, a tapped negative output of Balun is modulated into the optical domain and is launched to the optical delays and attenuators array for compensating the multipath effect between local transmitter and receiver. The optical delays and attenuators array are tuned precisely so that the best cancellation performance is obtained. Combination of the positive output and the negative output array is needed for subtraction. However, because each tap in the array are of the same wavelength, undesired signal beating will occur due to phase fluctuation in each of the branches. Thus, a SM-MM combiner is used to prevent signal degradation due to beating [19-20]. The recovered signal of interest is then detected by the multimode photodetector and converted back to the electrical domain.

3.3 Experimental Procedure and Results

In this experiment, we do a cable test to mimic multipath response. Here, a 0.12-meter path with a 2-dB attenuation and a 0.18-meter path with a 6-dB attenuation are combined together to setup the model. Figure 3.3 is the measured characteristic of the frequency response of our multipath effects model from 0 – 20 GHz. In order to duplicate this channel response for signal subtraction, an ICS with multiple compensation paths must be used. Since the multimode photodetector we used in the experiment has a limited bandwidth from 0 - 7 GHz, we will focus on multipath compensation from 0 – 7 GHz, as shown in

Figure 3.4. By adjusting each components in the optical delays and attenuators array, the compensation paths response closely match with the multipath response.

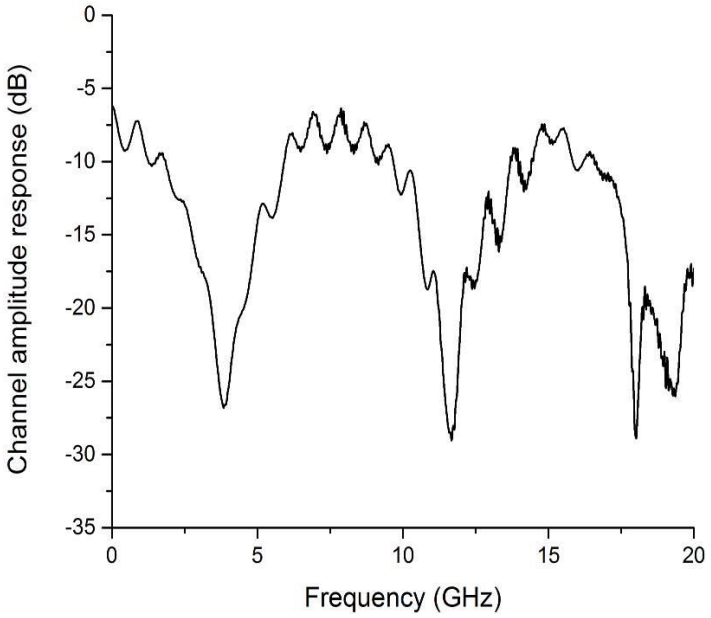

Figure 3.3. 0 – 20 GHz multipath model frequency response.

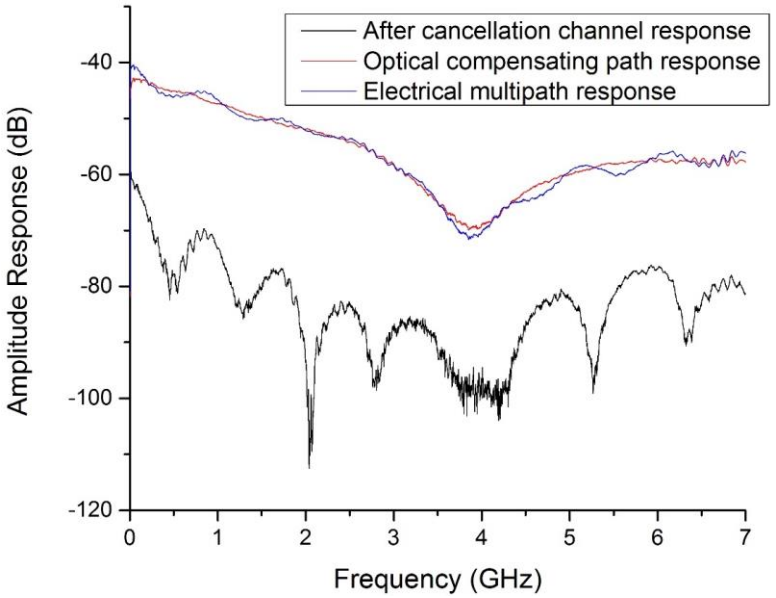

Figure 3.4. Comparison of frequency response between electrical multipath and compensating path.

To study the cancellation performance of the proposed multipath ICS, a network analyzer is used to measure the S21 response of the whole system and determine the cancellation depth over different frequency bands. The two EMLs are working at 1554.3 nm and 1553.7 nm respectively and have an output power of 3 dBm. An array of two precise optical delays with 0.03 ps resolution and two 16-bit digital controlled MEMS based optical attenuators is used to mimic and compensate the multipath response, so that the tapped interfering signal for subtraction can match the phase and amplitude of the received interfering signal. Output of the delays and attenuators array is combined with the signal from the upper branch (signal from the receiving antenna) through the single mode to multimode coupler and detected by the multimode photodetector. The cancellation depth over frequency is calculated by taking the S21 difference in dB between enabling and disabling the compensation array. The attenuations and delays are optimized to obtain the desired cancellation performance. A more than 20-dB cancellation over the whole 7 GHz bandwidth is experimentally obtained.

We also look at the cancellation performance for a narrower frequency band of interest. Figure 3.5 and Figure 3.6 illustrate the measured cancellation with its corresponding amplitude and phase mismatches over 800-MHz bandwidth at 2.4 GHz band. The 800-MHz bandwidth is chosen because it already exceeds the next generation wireless communication bandwidth requirement [21]. The absolute frequency response mismatch at 2.4 GHz over 800 MHz, both amplitude and phase, between the multi-path channel and the compensating array across the 800 MHz bandwidth are measured using the network analyzer and are plotted in Figure 3.5 (a)-(b) and Figure 3.6 (a)-(b). The best cancellation

over the frequency band is achieved when both the amplitude and phase mismatch approach close to zero.

With minor changes in the delay and attenuation settings in our system, different cancellation performance (frequency band, bandwidth, and cancellation) targeted for various applications have been demonstrated in Figure 3.5 (c) and 3.6 (c). The figures indicate a 40-dB cancellation over 200 MHz for wide bandwidth applications and a 50-dB cancellation over 40 MHz for narrow band applications.

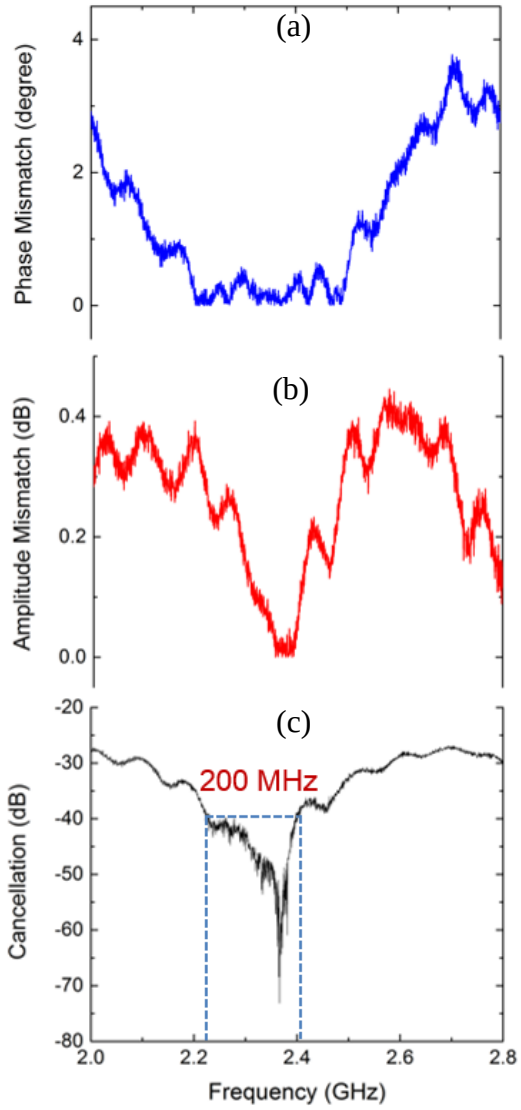

Figure 3.5. 40-dB cancellation over 200 MHz bandwidth at 2.4 GHz band. (a) Phase mismatch, (b) amplitude mismatch and (c) cancellation profile.

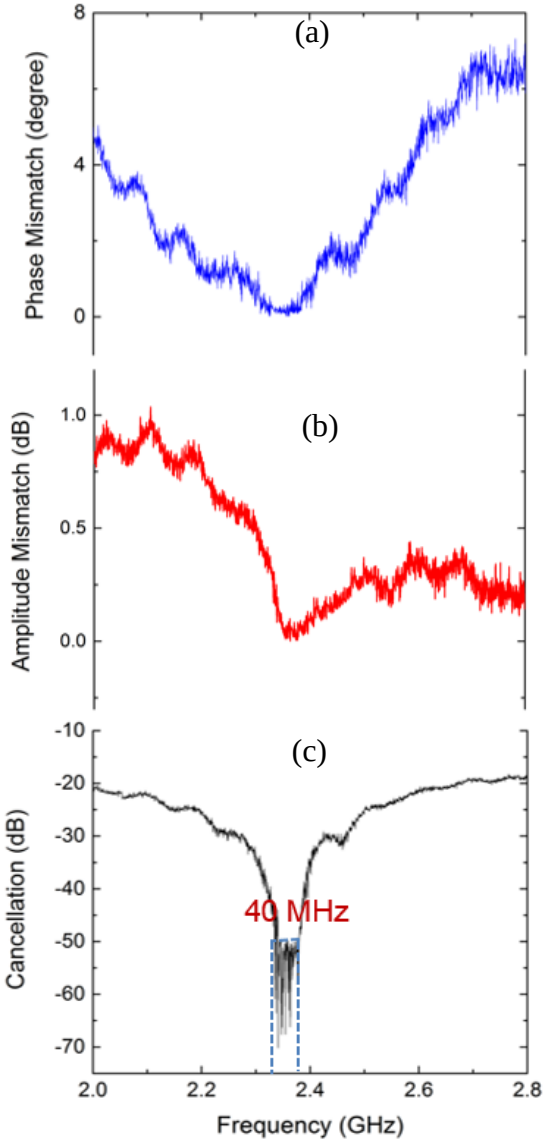

Figure 3.6. 50-dB cancellation over 40 MHz bandwidth at 2.4 GHz band. (a) Phase mismatch, (b) amplitude mismatch and (c) cancellation profile.

Furthermore, we have studied the cancellation performance during the recovery of a weak SOI which is masked by a strong interfering signal. A weak SOI that is only 15 dB above the noise floor and is 20 dB weaker that the interfering signal is used. The interfering signal and the SOI are generated from separate signal generators. The SOI is a weak single tone signal at 2.4 GHz and the interfering signal is a strong in-band signal at 2.4 GHz with

800-MHz bandwidth. They are combined together to mimic the overwhelmed interfered received signal.

Figure 3.7 demonstrates our system's performance in recovering the weak SOI from the dominant interfering signal. An RF spectrum analyzer is used to measure the spectrum before and after the cancellation of the strong interferer. The red curve in Figure 3.6 indicates the spectrum of the received signal consists of both the interfering signal and the signal of interest, the SOI is totally buried by the interfering signal and is not visible from the spectrum. The blue curve demonstrates the recovery of the weak SOI from the interfering signal, the optical delays and attenuators array is optimized such that residual interfering signal is minimal at the output spectrum. After cancellation, the weak SOI is now visible in the spectrum, we can further use an RF filter to suppress the residual interference.

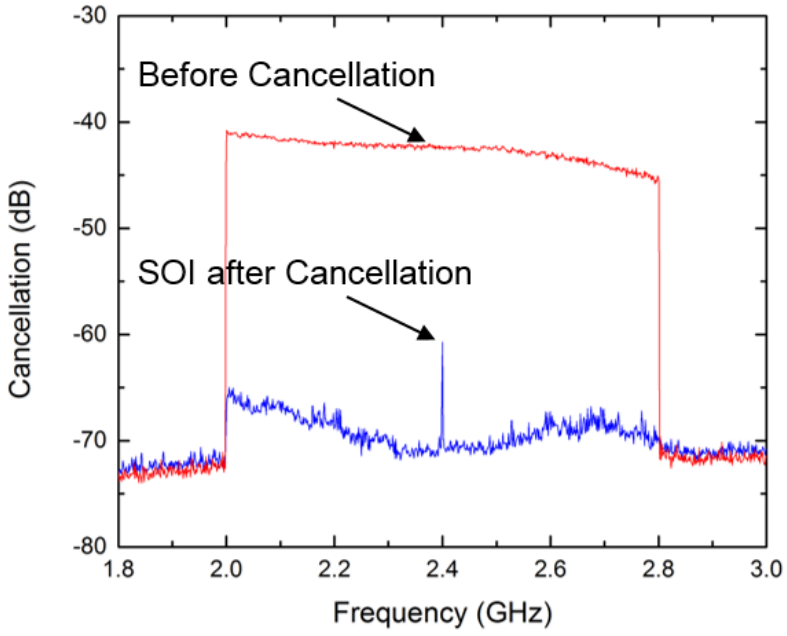

Figure 3.7. Measured RF spectrum of the received signal before interference cancellation (red curve) and after interference cancellation with hybrid multipath ICS (blue curve) at 2.4 GHz band.

According to the communication system requirements, both amplitude and phase modulation schemes have been adopted by different wireless communication systems. Moreover, phase modulation is essential to enable advanced modulation schemes for improved transmission capacity and performance. In the experiment, we also studied the cancellation performance when the SOI and interfering signal are both phase modulated instead of amplitude modulated. An electrical mixer is used to generate the PSK signal by launching an electrical data and an electrical carrier to the mixer. A 200 Mb/s signal from the bit-error-rate tester (BERT) is input to the intermediate frequency (IF) port of the mixer and a 2.4 GHz single tone signal is used as the local oscillator (LO). By properly setting the input power to the LO port as well as the IF port, a high quality eye diagram and a waveform have been generated as shown in Figure 3.8(a) and 3.9(a), respectively. The corresponding spectrum of the phase modulated signal is shown in Figure 3.8(b) and 3.9(b). We use an oscilloscope to measure the time domain response of the received signal before and after cancellation. Figure 3.10(a) is the eye diagram of the received signal before cancellation, both the weak phase modulated SOI and the stronger interfering signal are present in the time domain. After enabling our ICS, the interfering signal is removed out from the received signal, with the SOI fully recovered in the time domain as shown in Figure 3.10 (b).

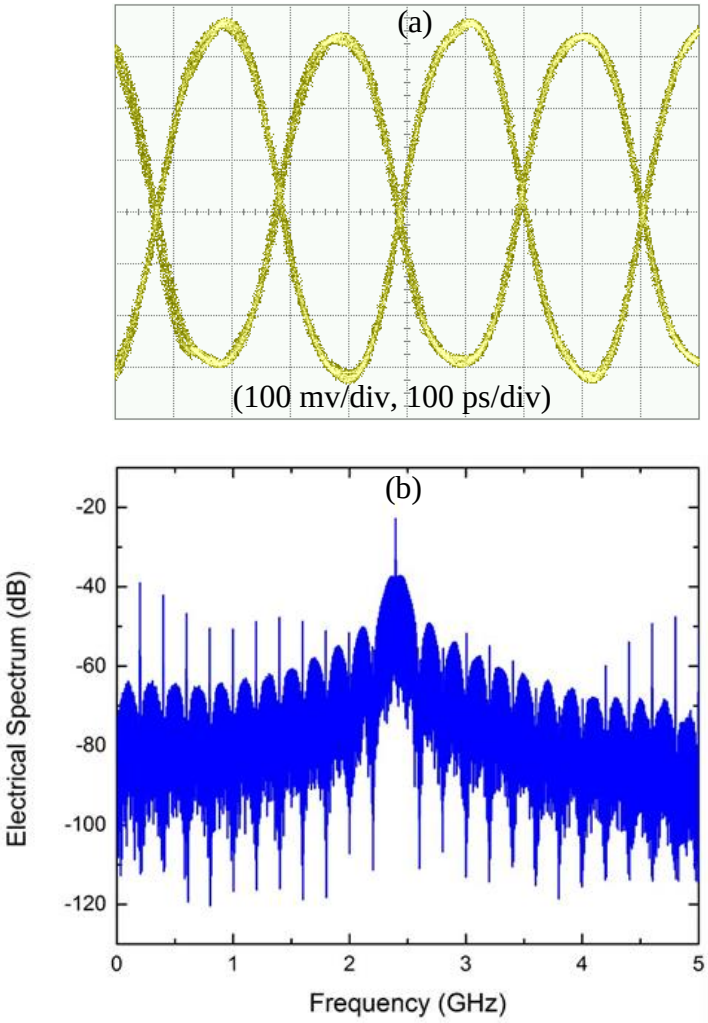

Figure 3.8. (a) Eye diagram and (b) electrical spectrum for 200 Mb/s phase modulated signal at 2.4 GHz.

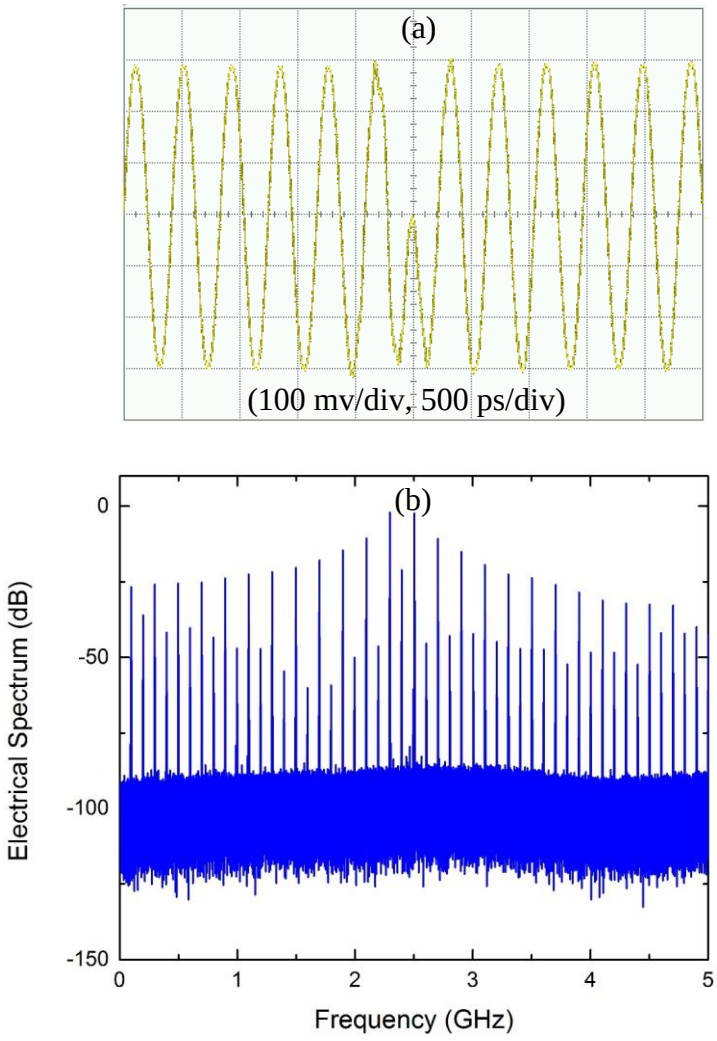

Figure 3.9. (a) Waveform and (b) electrical spectrum for 200 Mb/s phase modulated signal at 2.4 GHz.

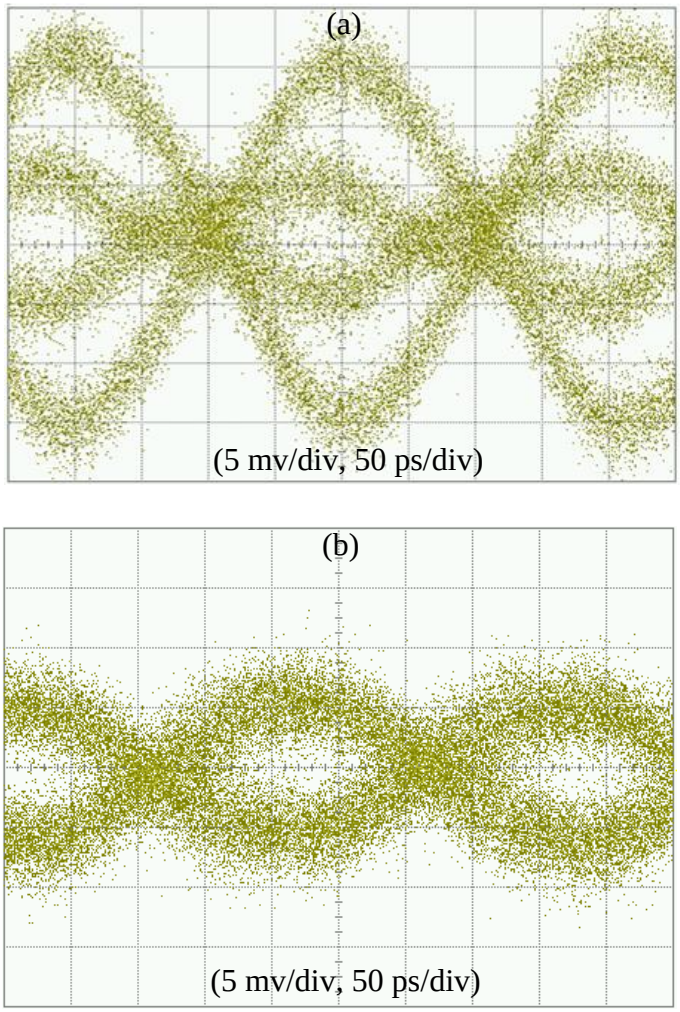

Figure 3.10. Eye diagram of received signal (a) before cancellation and (b) after cancellation.

Our system maintains decent performance for 900 MHz GSM band with only minor delay and attenuation adjustment needed. A 35-dB cancellation over 250 MHz bandwidth is demonstrated in Figure 3.11 (a). Moreover, a 2 GHz super-wide bandwidth cancellation from 0.5 – 2.5 GHz is obtained with more than 30 dB cancellation depth as shown in Figure 3.11 (b). Interference from multiple bands can be cancelled out simultaneously without any reconfiguration.

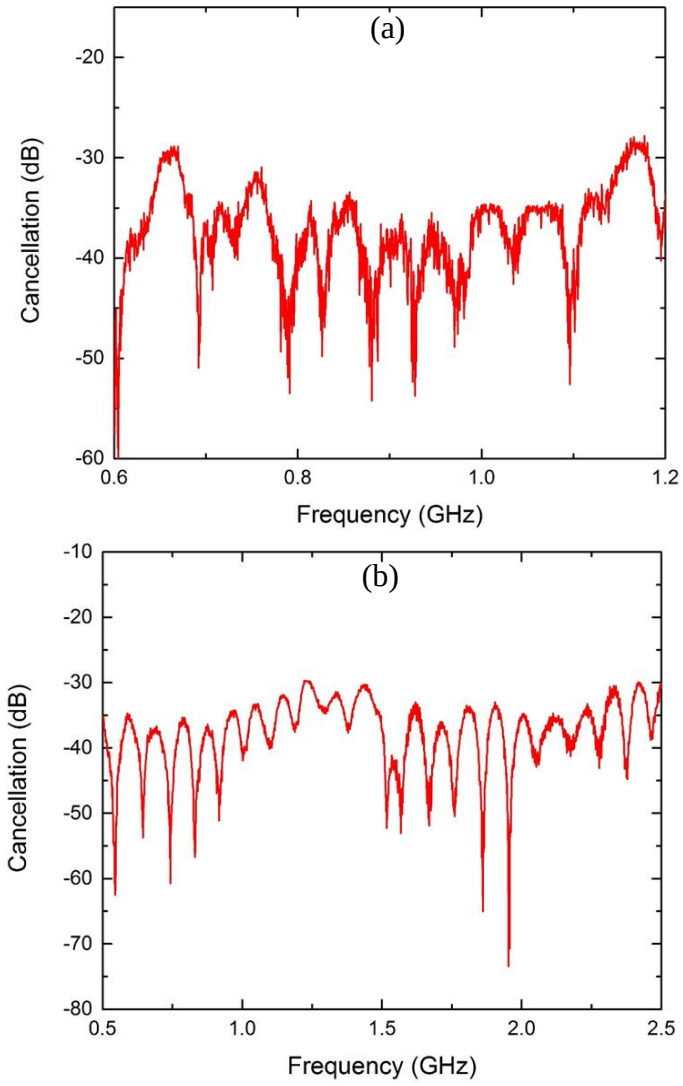

Figure 3.11. Measured cancellation performance of hybrid multipath ICS (a) with 600-MHz bandwidth at 900 MHz band, (b) with 2-GHz bandwidth at 1.5 GHz band.

We expanded our compensation array to include four sets of optical attenuators and delay lines to cancel out multipath interference with up to 3rd order multipath components. Here, the multipath model consists of four paths: 6 cm with 1-dB attenuation, 6 cm with 3-dB attenuation, 12 cm with 6-dB attenuation and 12 cm with 12-dB attenuation. Figure 3.12 demonstrates a 30-dB cancellation over 350 MHz at 1.5 GHz GPS band. This performance shows that our ICS is also capable of the harsher channel environment with more severe multipath effects.

In this chapter, we evolve our hybrid ICS for cancellation of multipath broadband interfering signals, so that only the signal of interest will be maintained. This improved approach is able to cancel out up to 4th order multipath components with decent cancellation performance. 50-dB cancellation over 40 MHz and 30-dB cancellation over 2 GHz are experimentally demonstrated. Our structure is capable for phase modulated interfering signal cancellation, the weak phase modulated SOI is fully recovered in the time domain.

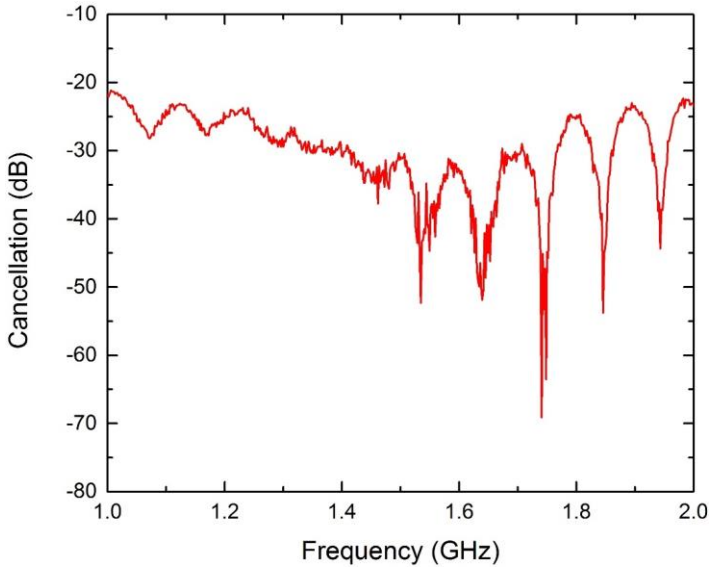

Figure 3.12. Measured 4-paths cancellation performance of hybrid multipath ICS with 1 GHz bandwidth at 1.5 GHz band.

CHAPTER 4

DYNAMIC INTERFERENCE CANCELLATION SYSTEM

4.1 Introduction

Channel response of a wireless channel is dynamic especially if the antenna are mobile. In the scenario where the transmitting antenna and receiving antenna are co-located on the same vehicle, the distance between the two antennas are roughly fixed, but there are minor changes due to the vibration of the vehicle. The wireless channel between the transmitting antenna and receiving antenna has a short coherence time on the order of ms because of the motion and vibration of the vehicle, which makes the traditional motorized and thermal tuning delay incapable and cost-effective to incorporate with interference cancellation system for subtracting the variate interferers. A fast tunable optical delay is required to achieve the dynamic ICS system for tackling vulnerable channel response.

Tunable optical delays are fundamental building blocks in optical signal processing, however, their tuning speeds are usually slow. Several categories of tunable delay are proposed based on different theories. Ring-resonator based tunable delay offers us continuous tunability and a small footprint [22-23]. However, the group delay appearing at resonant frequencies are tuned using slow thermal effects, while a significant insertion loss is also introduced. Another approach based on spatial light modulators, although useful for mimicking true-time delay through arbitrary filter generation, the application range is limited by the slow speed of the filter generation [24]. Besides, other existing approaches

based on switches can only offer discrete time delay [25], which will significantly degrade the cancellation depth of the ICS. Delay based on highly dispersive fiber [26] or fiber bragg gratings [27] are able to offer continuous wide range tunable delay. However, as the delay is controlled by the slow tuning of laser frequency, limiting the tuning speed to the millisecond range.

In this chapter, we propose and experimentally demonstrate a fast tunable delay structure based on the slow and fast light effect in semiconductor optical amplifier (SOA). Continuous delay of up to 200 ps is obtained through controlling the optical pump power. In the later part of this chapter, we incorporate the fast tunable delay with the hybrid ICS to enable dynamic co-site co-channel interference cancellation. A 50-dB cancellation over 40 MHz is experimentally achieved.

4.2 Fast Tunable Delay

Slow and fast light effect is based on the changing of the group velocity. The group velocity of light (V_g), is given by the following formula [28]:

$$V_g^{-1} = \frac{dk(\omega)}{d\omega} = \frac{1}{c}\left[n(\omega) + \omega\frac{dn(\omega)}{d\omega}\right] \tag{4.1}$$

Here, $\boldsymbol{\omega}$ is the angular frequency of the light wave, k is the wave factor and c is the light speed. As shown in the formula, the group velocity is determined by the rapid change in refractive index, $dn(\boldsymbol{\omega})/d\,\boldsymbol{\omega}$. In the SOA, this process is achieved via coherent population oscillations (CPO) [29]. The CPO effect is obtained through the direct interference between the pump and probe. The interference will generate the coherent spectral hole in the SOA and leads to a large change of refractive index.

Figure 4.1 illustrates the system structure of the SOA based fast tunable delay. A microwave signal is modulated onto an EML with a carrier wavelength at 1553.7 nm to work as the probe and launches into the SOA via an optical circulator. A unmodulated cw light at higher power acts as the pump, enter the SOA via another optical circulator from the other side. The pump and probe are counterpropagating through the SOA to improve the isolation between pump and probe at the output. Based on the CPO effect, the $dn(\omega)/d\omega$ is positive, which results in a decreased group velocity, such that a delay on the probe is obtained. After exiting the SOA, the probe is passed through a circulator and a bandpass filter for suppressing undesired noise, and then detected by the photodetector for converting it back to electrical domain. The output microwave signal is compared to itself with different pump power by a network analyzer to determine the relative delay over pump power. The pump power is swept from -20 dBm to 10 dBm.

Figure 4.2 (a) shows the measured delay over different pump powers, the value is normalized to the delay at pump power of -20 dBm. As shown in this figure, up to a 200 ps delay can be obtained via changing the pump power from -20 dBm to 10 dBm. An amplitude shift is observed at different pump powers due to cross gain modulation in the

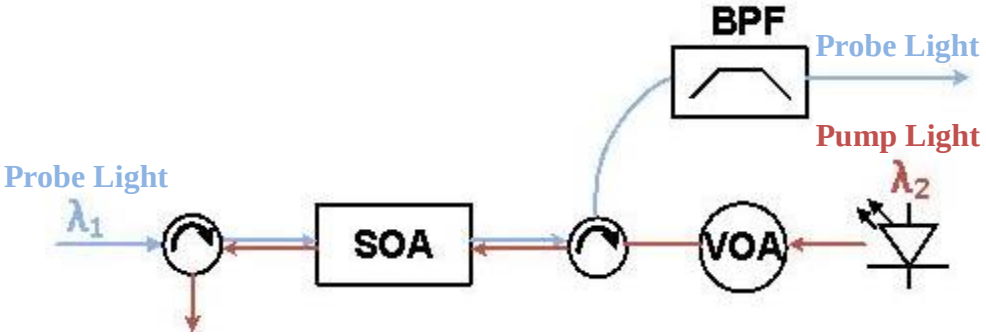

Figure 4.1. Structure of fast tunable delay. λ_1 = 1553.7 nm, λ_2 = 1550.1 nm, SOA: semiconductor optical amplifier; VOA: variable optical attenuator; BPF: band pass filter.

SOA. The corresponding amplitude shift is normalized to the amplitude when the pump power is at -20 dBm and is plotted in Figure 4.2 (b), which can be compensated through an optical attenuator.

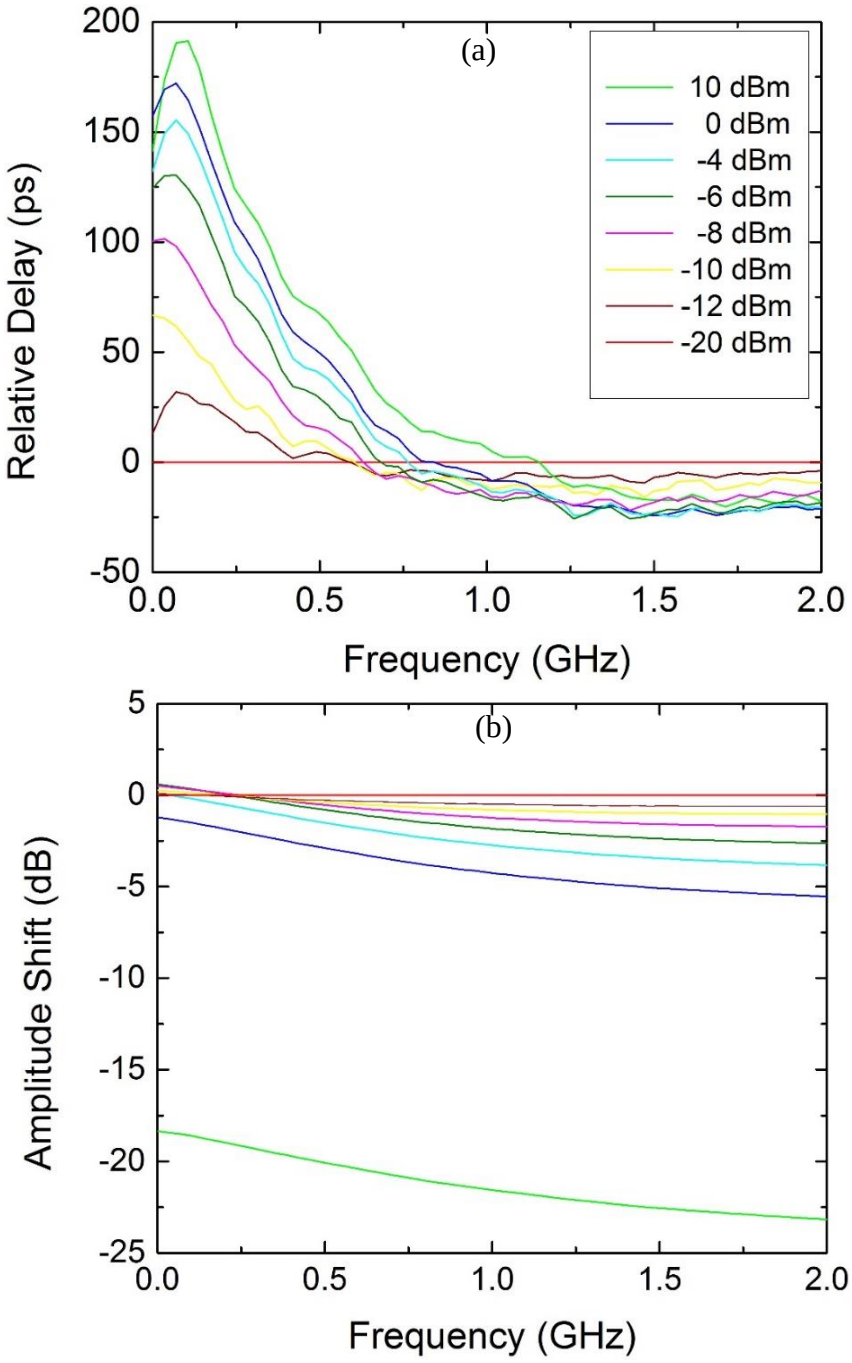

Figure 4.2. Relative delay (a) and amplitude shift (b) introduced by SOA with different pump power.

4.3 Experimental Procedure and Results for Dynamic ICS

The dynamic interference cancellation system subtracts the in-band co-site interferer from the corrupted received signal. The system accepts the corrupted received signal and a tap of the interfering signal as the inputs, and it outputs the recovered signal of interest at the dynamic ICS output as illustrated in Figure 4.3.

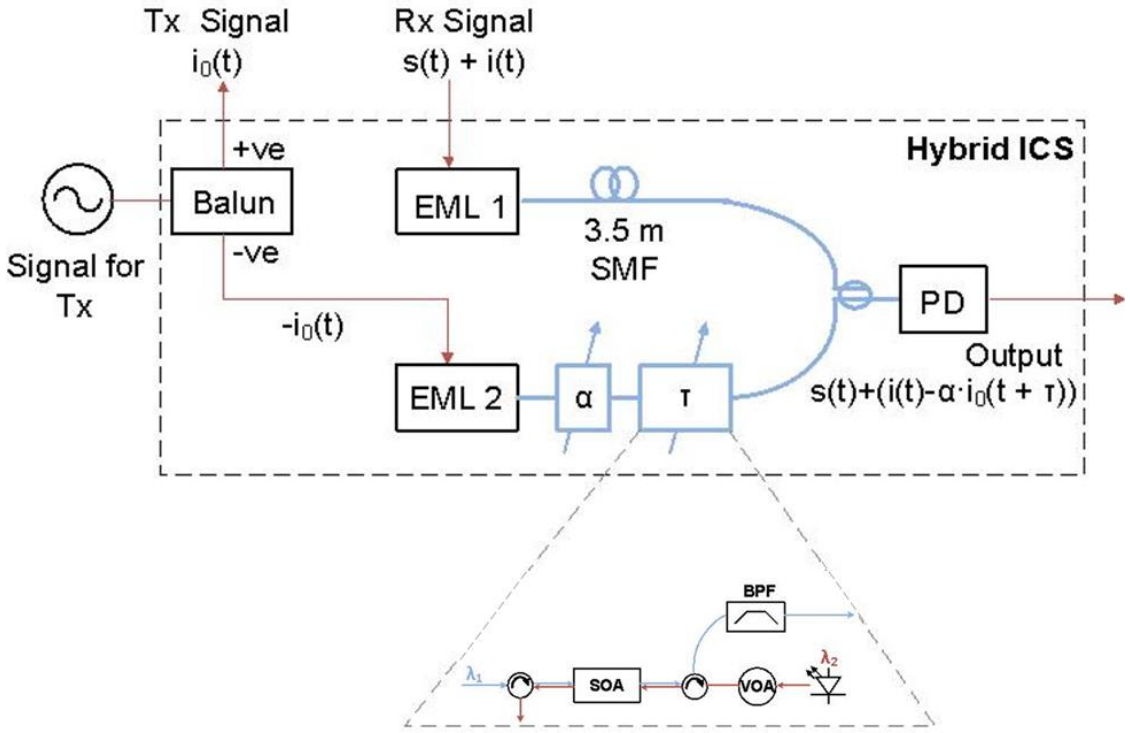

Figure 4.3. Schematic illustration of the dynamic ICS. Blue thick lines: Optical paths. Thin red lines: electrical paths. Tx: transmitter; Rx: receiver; RF balun transformer; EML 1-2: electro-absorption modulated lasers; α: tunable optical attenuator; τ: fast tunable delay; SMF: standard single mode fiber; PD: photodetector.

We experimentally study the performance of the dynamic ICS. A network analyzer is used to measure the S21 response for determining the cancellation depth and bandwidth.

The two EMLs are operating at 1554.3 and 1553.7 nm, respectively, and have an output power of 0 dBm to prevent the damage on photodetector after amplification. The proposed fast tunable delay is incorporated into the lower branch for offering fast tuning delay/phase optimization through precisely adjusting the optical pump power, while a precise fast tunable optical attenuator is used to compensate the power/amplitude mismatch. The optical signal from both the upper and lower branches are combined through a 3 dB optical coupler and detected by the photodetector.

To determine the amount of cancellation, we first disable the lower branch of the dynamic ICS, such that we can measure the interfering signal level before cancellation, indicated as $S21_{before}$. Then the lower branch is reconnected to measure the power of the residual interference after cancellation, indicated as $S21_{after}$. By taking the difference of $S21_{before}$ and $S21_{after}$ in dB, the cancellation depth is determined. Figure 4.4 demonstrates the dynamic ICS ability to cancel the co-site co-channel interference and illustrate how the fast tunable delay is used to dynamically converge to minimum residual interference. In

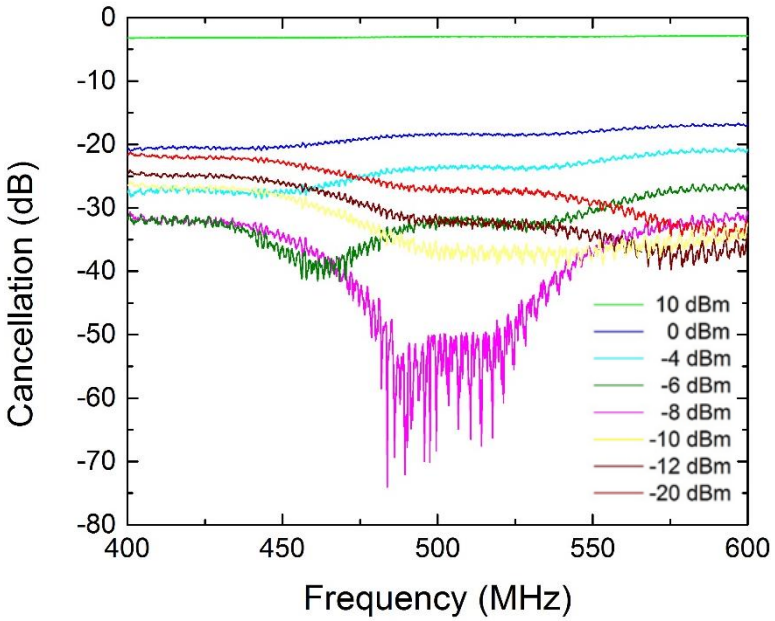

Figure 4.4. Cancellation Performance Comparison with different pump power.

this figure, the cancellation performance centered at 500 MHz over a 400 MHz bandwidth is measured under eight states of the fast tunable delay, with each one specifying its pump power. As the delay is tuned across those states, the dynamic ICS reaches a maximum of 50-dB cancellation over 40 MHz, which is very useful for land mobile services working at 500 MHz band. The absolute amplitude and phase mismatch as well as the cancellation profile of the best cancellation performance among the 8 states are measured and demonstrated in Figure 4.5.

The weak signal of interest (SOI) is masked by the strong interferer as discussed in former chapters, a weak SOI which is ~ 15 dB above the noise floor and a strong interfering signal which is ~ 20 dB stronger than SOI are generated separately by individual signal generators and coupled together to mimic the corrupted received signal. The SOI is a single tone signal at 500 MHz while the interfering signal is a strong in-band signal with 200 MHz bandwidth.

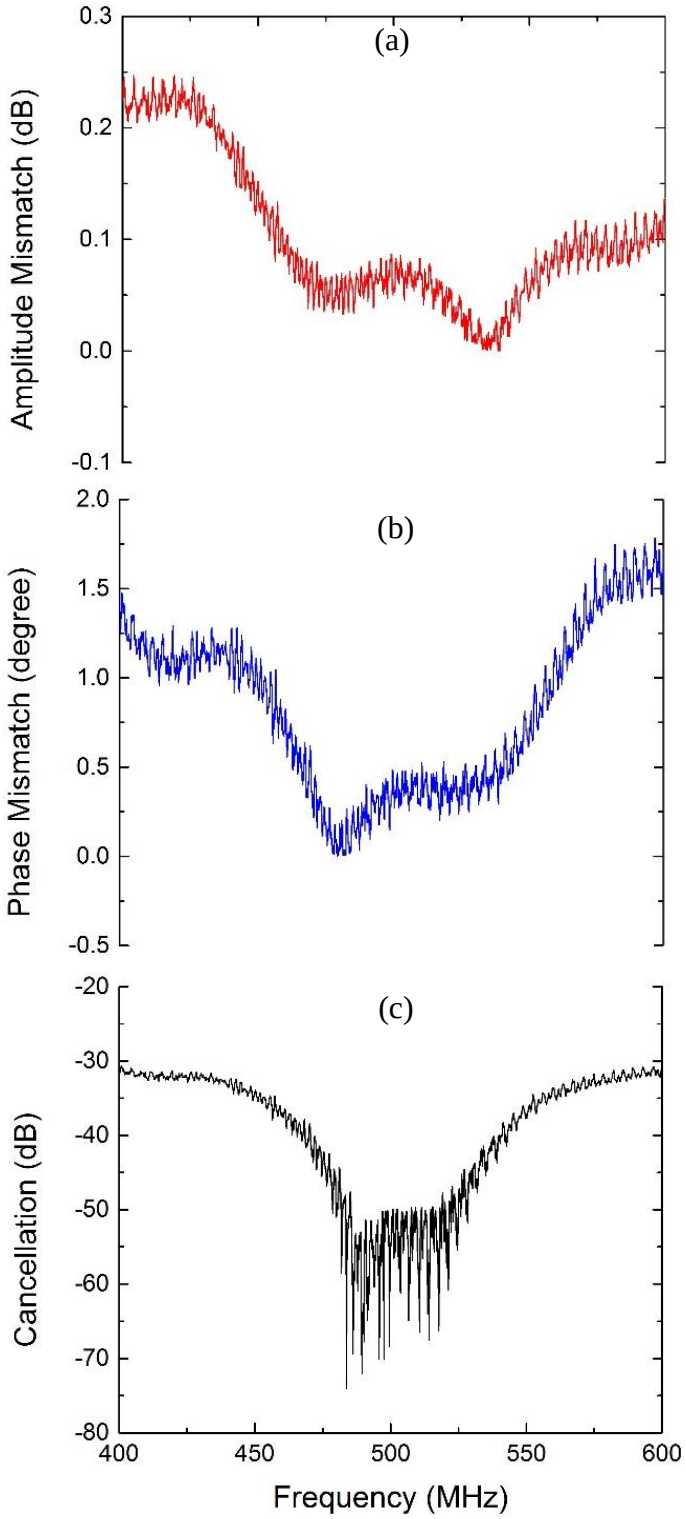

Figure 4.5. Absolute amplitude (a) and phase (b) mismatch as well as cancellation profile of the dynamic ICS at 500 MHz band.

Figure 4.6 show the ICS spectral performance in recovering the weak SOI using the fast tunable optical delay. An RF spectrum analyzer is used for measurement. The red curve in Figure 4.7 is the measured received signal, which consists of both the strong interfering signal and the weak SOI. The weak SOI is completely buried by the in-band interfering signal as shown. To cancel out the 200 MHz strong interfering signal, the dynamic ICS is enabled, and the fast tunable delay is tuned, such that the residual interfering signal is minimum at the output. The resultant signal after cancellation is shown by the blue curves in this figure. The SOI is now recovered from the received signal, and is clearly shown in the resultant RF spectrum.

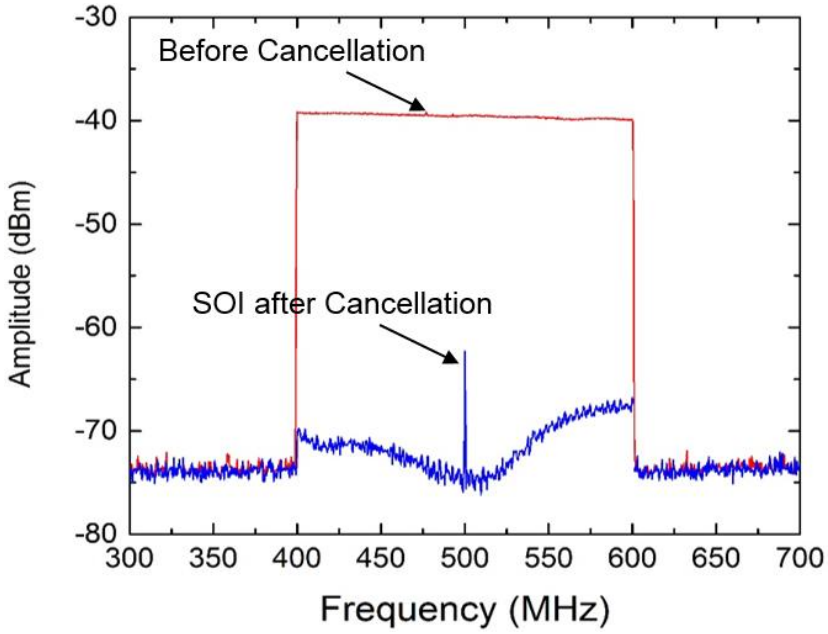

Figure 4.6. Measured RF spectrum of the received signal before interference cancellation (red curve) and after interference cancellation with dynamic ICS (blue curve) at 500 MHz band.

4.4 Summary

In this chapter, we proposed and experimentally demonstrate a dynamic interference cancellation system using SOA based fast tunable delay. The fast tunable delay offers up to a 200 ps delay, while the dynamic ICS obtains a 50-dB cancellation over 40 MHz bandwidth. The fast tunable delay is controlled by optical pump power, making it capable for fast convergence and helps the system to maintain the best cancellation performance in a vibrating channel environment.

CHAPTER 5

MICROWAVE PHOTONIC MIXER

5.1 Introduction

To meet the requirements of the increasing data-rates, it's essential to design a system which has the capability of advanced modulation schemes and can be incorporated with the proposed interference cancellation system, such that a high transmission capacity simultaneously transmitting and receiving functions are available. Due to the broadband, high-capacity, and low-loss characteristics of fiber optics, radio-over-fiber (RoF) techniques are the most efficient way to distribute and transmit high-speed multimedia signals. To meet the growing demand of high data-rate wireless communications as well as to fully utilize the capacity of optical fibers, microwave photonic signal processing techniques have attracted lots of research interest [30]. In RoF, the microwave signal is first modulated onto a high-frequency carrier (usually refers as the local oscillator (LO)) with an electrical mixer, and then this modulated signal is used to modulate the optical carrier for transmitting in the optical fiber. Due to the increasing data-rate demanded by the high-speed wireless system as well as the corresponding high-frequency carrier needed, the frequency requirement reaches the bandwidth limitation of electrical mixer. With the broadband and low loss characteristic of photonics, photonics based microwave mixer can realize ultra-wideband mixing operation and can support RF signal and LO that are at distributed locations. Due to the high isolation provided by photonic components, the

microwave photonic mixer has an infinite isolation between RF, IF, and LO ports [31] which is a desired feature in most microwave system. Various approaches for demonstrating a microwave photonic mixer have been proposed, including the use of cascading Mach-Zehnder modulators (MZM) [32], a dual-parallel MZM [33], dual-wavelength phase modulation followed by optical filtering [34], single-wavelength phase modulation with stimulated Brillouin scattering for carrier suppression [31], as well as single sub-carrier modulation together with LO mixing from a separate optical path [35-38]. However, the existing approaches either have low conversion efficiency, suffer from the disability of phase modulation, or require complicated off-line digital signal processing for compensating the phase incoherence between carriers. Recently, a photonic microwave mixing technique based on coherent orthogonal optical carriers' generation has been demonstrated [39], which solves the challenges mentioned above. However, spectral filtering is required during coherent orthogonal carriers generation which hinder the ability to tune the LO frequency as well as set a limit to the lowest possible frequency for the LO.

5.2 Theory and Method of Operation

As such, the following work is drawn from our submitted manuscript to IEEE Photonics Technology Letters on 05/27/2015 by Qi Zhou and Mable P. Fok entitled, "Microwave Photonic Mixer based on Polarization Rotation and Polarization Dependent Modulation," in which we present and experimentally demonstrate a microwave photonic mixer that works well for both amplitude and phase modulation without the need of complicated off-line processing for phase compensation or an optical filter that limits the LO frequency

range. The elimination of an optical filter removes the lower frequency limit imposed on the LO as well as enables flexible tuning of LO frequency. The ability to tune the LO frequency can potentially enable dynamic spectral access and enhance transmission security. Principle of the proposed optical mixer is based on the use of single-sideband modulation in a dual-drive MZM followed by polarization rotation in semiconductor optical amplifier (SOA). Both the power of the single-sideband signal and the SOA bias current are optimized, such that when a single-sideband signal is launched into the SOA, the phase shift is the same for both the transverse-electric (TE) and transverse-magnetic (TM) modes of the carrier, however, the $+1^{st}$ order sideband will have a different phase shift between its TE and TM mode [40]. Thus, polarization angle discrepancy between the optical carrier and the $+1^{st}$ order sideband is resulted and a pair of phase coherent carriers with different polarization is obtained. The proposed scheme can support a wide range of frequency [41] that is governed by the modulator bandwidth, which significantly extends the lower frequency range of the LO as well as improves the frequency tunability of the LO. In this letter, we are demonstrating up-conversion where a LO is mixing with an intermediate frequency (IF) signal such that a radio frequency (RF) signal is resulted. The MZM for modulating the IF signal onto the optical carrier is polarization sensitive, such that TE and TM axis of the MZM have different modulation efficiencies. As a result, the IF signal will mainly be modulated onto the $+1^{st}$ order sideband by aligning it to the high modulation efficiency axis in the MZM. Due to the phase coherence of the optical carrier and $+1^{st}$ order sideband, our approach supports both amplitude modulation and phase modulation. With the proposed scheme, we have successfully demonstrated the modulation of phase stable binary-phase-shift keying (BPSK), amplitude-shift keying

(ASK) and on-off keying (OOK) signals. Widely opened eye diagrams and clear waveforms are obtained for all of the modulation formats.

Figure 5.1 shows the experimental setup of the proposed microwave photonic mixer for up-conversion. A distributed feedback (DFB) laser at λ_c is used as the light source for modulation in the dual-drive Mach-Zehnder modulator (DDMZM). Sinusoidal microwave signal f_{LO} is used as the LO, which is launched to the DDMZM via a 90 ° hybrid coupler. By properly setting the bias voltage applied to the DDMZM, single-sideband modulation with more than 30-dB suppression on the -1st order sideband is obtained. The optical fields of the carrier and +1st order sideband are governed by

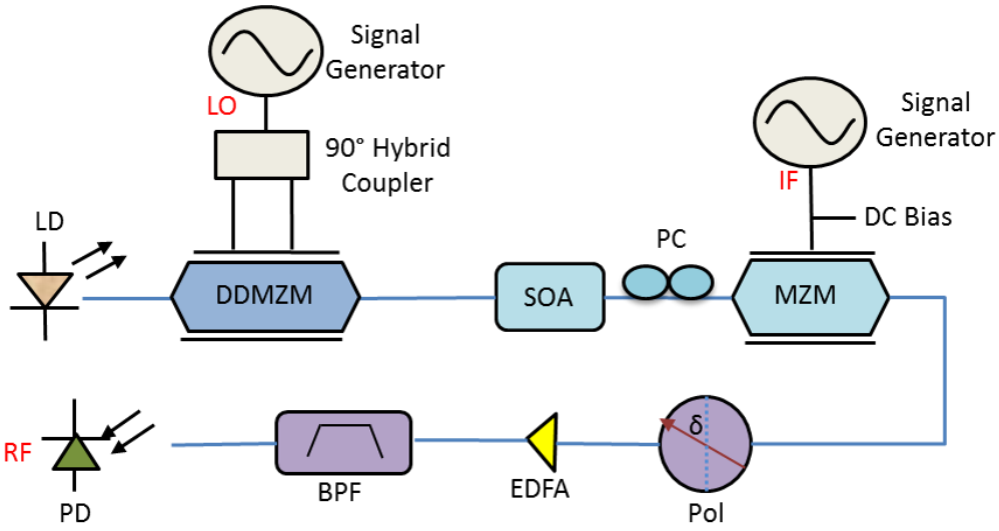

Figure 5.1. Experimental setup of the microwave photonic mixer. LD: laser diode. DDMZM: dual-drive Mach-Zehnder modulator; SOA: semiconductor optical amplifier; PC: polarization controller; MZM: Mach-Zehnder intensity modulator; Pol: polarizer; EDFA: Er-doped fiber amplifier; BPF: bandpass filter; PD: photodetector; LO: local oscillator; IF: intermediate frequency. RF: radio frequency.

$$\begin{pmatrix} \boldsymbol{E_c(t)} \\ \boldsymbol{E_s\,(t)} \end{pmatrix} = \begin{bmatrix} E_c \cdot e^{j(\omega_c t + \varphi_0)} \\ E_s \cdot e^{j\omega_s t} \end{bmatrix} \tag{5.1}$$

$\boldsymbol{E_c(t)}$ and $\boldsymbol{E_s(t)}$ are the optical fields of the carrier and the +1st order sideband respectively, while E_c and E_s are the corresponding amplitudes of the optical fields. ω_c, ω_s and φ_0 are the optical frequencies of the carrier and +1st order sideband, and the initial phase difference between them, respectively. Figure 5.2 illustrates polarization evolution of the carrier and the +1st sideband in SOA as well as during IF modulation process in MZM. TE and TM are the axis of the SOA, and the output of the DDMZM at 5 dBm is launched to the SOA at a polarization angle of α with respect to the TM axis of SOA. Phase shift induced onto the carrier is the same for both TE and TM modes, while the phase shift

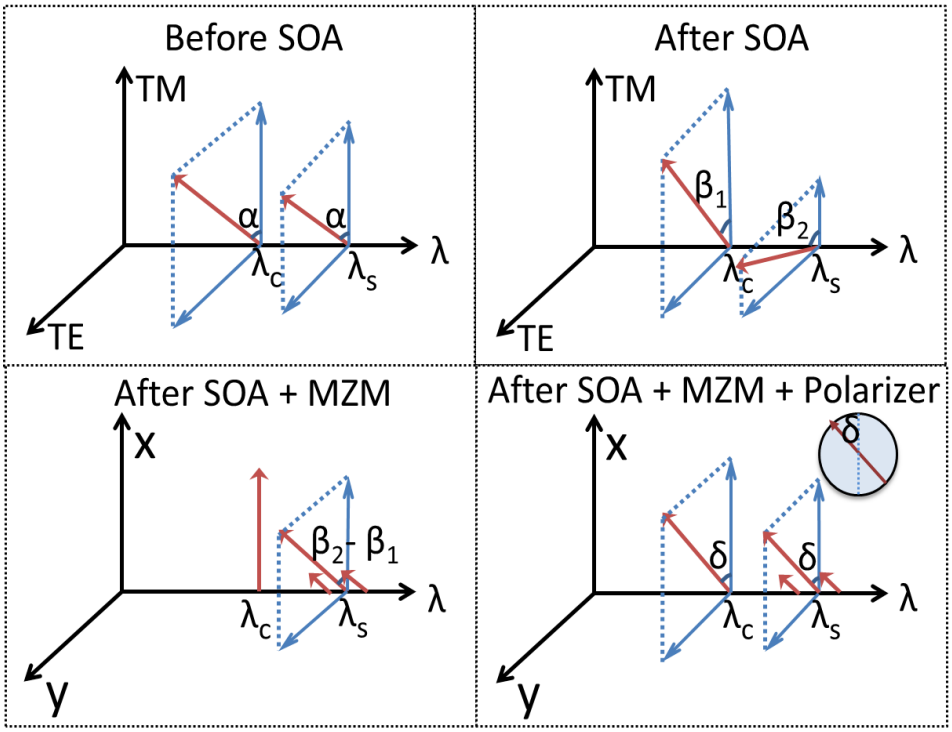

Figure 5.2. Principle of the proposed microwave photonic mixer based on polarization rotation in SOA.

induced onto the +1st order sideband are different for the TE and TM mode [36]. Thus, there is a polarization rotation in the +1st order sideband relative to the polarization of the carrier, resulting in a new polarization angle of β_1 and β_2 for the carrier and +1st order sideband with respect to the TM axis of the SOA, respectively. Ideally, polarization between the carrier and the +1st order sideband should be orthogonal to obtain the best modulation performance by the IF. The MZM for IF modulation also consists of both TE and TM axis, we refer the two axis as x and y. Then, we align the output signal of SOA to the MZM axis such that the carrier is aligned with the x axis. Thus, output from the SOA can be expressed as:

$$\begin{pmatrix} \boldsymbol{E_{out-c}(t)} \\ \boldsymbol{E_{out-s}(t)} \end{pmatrix} = \begin{bmatrix} E_{c-x} \cdot e^{j(\omega_c t + \varphi_0)} \\ E_{s-x} \cdot e^{j\omega_s t} + E_{s-y} \cdot e^{j\omega_s t} \end{bmatrix} \tag{5.2}$$

$\boldsymbol{E_{out\text{-}c}(t)}$ and $\boldsymbol{E_{out\text{-}s}(t)}$ are the output fields of the SOA at optical frequency ω_c and ω_s. $E_{c\text{-}x}$, $E_{s\text{-}x}$ and $E_{s\text{-}y}$ represent the field amplitudes of the carrier and sideband at polarization axis x and y, respectively. Output signal of the SOA, which is the pair of phase coherent carriers is aligned to the MZM axis such that the carrier polarization is aligned with the x-axis that has minimum modulation efficiency, while the +1st order sideband polarization is aligned close to the y-axis such that it experiences a significantly efficient modulation. IF signal at f_{IF} is applied to the MZM and the optical field can be written as

$$\begin{pmatrix} \boldsymbol{E}' \boldsymbol{_{out-c}(t)} \\ \boldsymbol{E}' \boldsymbol{_{out-s}(t)} \end{pmatrix} = \begin{bmatrix} E_{c-x} \cdot e^{j(\omega_c t + \varphi_0)} \\ E_{s-x} \cdot e^{j\omega_s t} + E'_{s-y}(t) \cdot e^{j(\omega_s t + \partial(t))} \end{bmatrix} \tag{5.3}$$

where $\boldsymbol{E'_{out\text{-}c}(t)}$ and $\boldsymbol{E'_{out\text{-}s}(t)}$ represent the fields of the carrier and +1st order sideband at the output of the MZM. $E_{s-y}^{'}(t)$ and ∂(t) are the intensity and phase modulation on the +1st order sideband, respectively. A polarizer is placed after the MZM and has its polarization angle (δ) aligned in between the two polarization states of the carrier and +1st order sideband, such that the polarization component at δ is extracted from both the carrier and +1st order sideband for beating at the photodetector (PD). The optical process is completed at this point and the resultant signal at polarization δ can be expressed as:

$$\boldsymbol{E_{\delta}(t)} = E_{c-\delta} \cdot e^{j(\omega_c t + \varphi_0)} + E_{x-\delta} \cdot e^{j\omega_s t} + E_{y-\delta}(t) \cdot e^{j[\omega_s t + \partial(t)]} \qquad (5.4)$$

where δ is the optimized polarization angle of the polarizer with respect to the x axis and $\boldsymbol{E_{\delta}(t)}$ represent the output field of the polarizer. $E_{c\text{-}\delta}$, $E_{x\text{-}\delta}$, $E_{y\text{-}\delta}(t)$ are the amplitudes of the δ polarization component of the carrier and +1st order sideband along the x- and y-axis. The measured optical spectrum after the polarizer is depicted in Figure 5.3(a), which shows that the IF signal is only modulated onto the +1st order sideband (indicated by the sub-sideband around λ_s) but not the carrier. An Er-doped fiber amplifier is used to provide amplification while a 0.4nm band-pass filter is used to suppress the amplified-spontaneous-emission noise. A 10-GHz photodetector is used to convert the optical signal back to electrical domain. According to the square law detection, the photocurrent is governed by:

$$I_{PD} \sim \boldsymbol{E_{\delta}}(t) \cdot \boldsymbol{E_{\delta}^{*}}(\mathrm{t})$$

$$= \underbrace{E_{c-\delta}^{2} + E_{x-\delta}^{2}}_{\text{DC Component}} + \underbrace{2 \cdot E_{c-\delta} \cdot E_{y-\delta}(t) \cdot \cos[2\pi f_{LO} t + \varphi_0 - \partial(t)]}_{\text{Mixing Signal}}$$
$$+ \underbrace{2 \cdot E_{c-\delta} \cdot E_{x-\delta} \cdot \cos[2\pi f_{LO} t + \varphi_0]}_{\text{LO}}$$
$$+ \underbrace{2 \cdot E_{x-\delta} \cdot E_{y-\delta}(t) \cdot \cos[\partial(t)] + E_{y-\delta}^{2}(t)}_{\text{Baseband Signal}} \qquad (5.5)$$

where $\boldsymbol{E_{\delta}^{*}}(\mathrm{t})$ is the conjugate of $\boldsymbol{E_{\delta}(t)}$ and f_{LO} is the newly generated microwave signal, which equals to the optical frequency difference between the carrier and the +1st order sideband. As shown in equation (5), the mixing signal indicated as $2 \cdot E_{c-\delta} \cdot E_{y-\delta}(t) \cdot \cos[2\pi f_{LO} t + \varphi_0 - \partial(t)]$ has been produced. With the PD, the intensity and phase that were modulated on the +1st order sideband at the MZM are now converted to the intensity and phase modulation of the generated electrical carrier f_{LO}. Electrical spectrum of the PD output is shown in Figure 5.3(b). New frequency components at f_{LO}, $f_{LO} - f_{IF}$ and $f_{LO} + f_{IF}$ have been generated, indicate that frequency mixing and signal modulation are achieved. Figure 5.3 (c) is the PD output measured by a 40-GHz oscilloscope when no IF signal is being applied to the MZM. A clear sinusoidal waveform with stable amplitude has been generated, which indicates that the phase coherence between the optical carrier and the +1st order sideband has been maintained throughout the whole system.

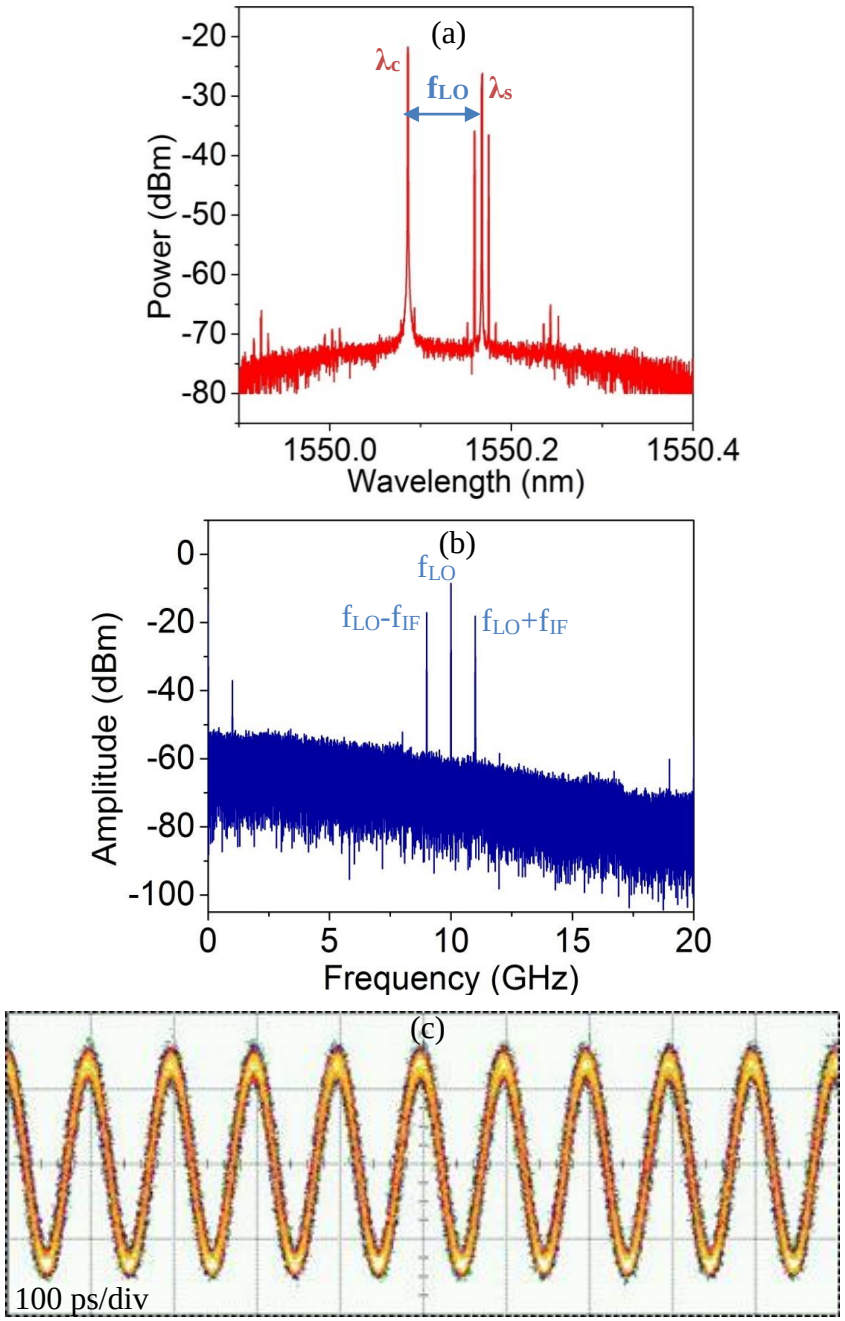

Figure 5.3. (a) Optical spectrum measured after the polarizer. (b) Electrical spectrum of the PD output. (c) Waveform of the LO with the frequency at 10 GHz.

5.3 Performance of Microwave Photonic Mixer

To investigate the performance of the proposed microwave photonic mixer, we first study ASK and OOK modulations onto a 10-GHz microwave carrier. A 10-GHz sinusoid microwave signal is generated from a signal generator and is used to drive the DDMZM as a LO. A 1-Gbps 2^{15}-1 pseudo-random-bit-sequence (PRBS) signal is used as the IF signal, which is used to drive the polarization sensitive MZM. Polarization of the input light is set such that the carrier is aligned with the MZM axis with minimum modulation efficiency, such that the PRBS signal is modulated onto the $+1^{st}$ order sideband but not the carrier. The MZM is biased at the positive slope of the transmission curve, where bit-0 voltage level is aligned with the minimum transmission point of the MZM. Thus, an OOK modulation is obtained on the 10 GHz LO after being detected by the PD. Widely-opened eye diagrams of the modulated signal are resulted and are shown in Figure 5.4(a)-5.4(b). Fig. 5.4(a) is the eye diagram showing four complete bits in the PRBS signal, while Fig. 5.4(b) is the zoom-in view within one bit. When an eight-bit bit sequence of 11010010 is applied to the MZM as an IF signal, a clear waveform is shown in Figure 5.4(c) while a zoom-in view is shown in Figure 5.4(d). Both Fig. 5.4(c)-5.4(d) clearly indicate OOK modulation of the 10-GHz LO is successfully achieved and a conversion efficiency of 3-dB is obtained. To achieve ASK modulation, the MZM for IF modulation is biased at a point on the positive slope such that bit-0 voltage level is aligned slightly away from the minimum transmission point of the MZM. Both a PRBS signal and a 11010010 sequence are used as the IF signals. Widely opened eye diagrams and clear waveforms are obtained as shown in Fig. 5.5(a) – 5.5(d), indicating ASK modulation of the LO is achieved.

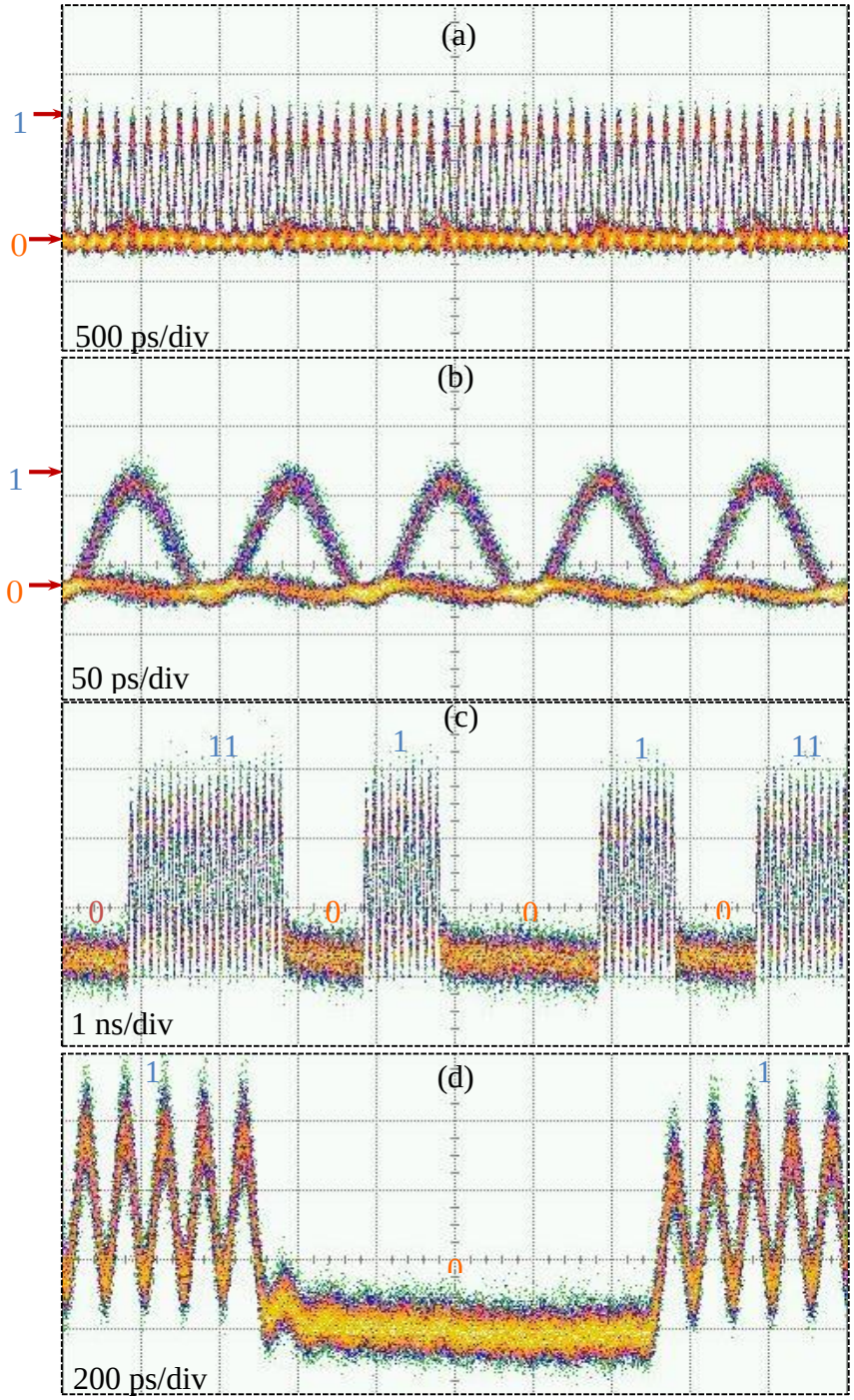

Figure 5.4. (a)-(b) Eye diagrams of PRBS OOK modulation at 1-Gbps; (c)-(d) 11010010 bit sequence OOK modulation.

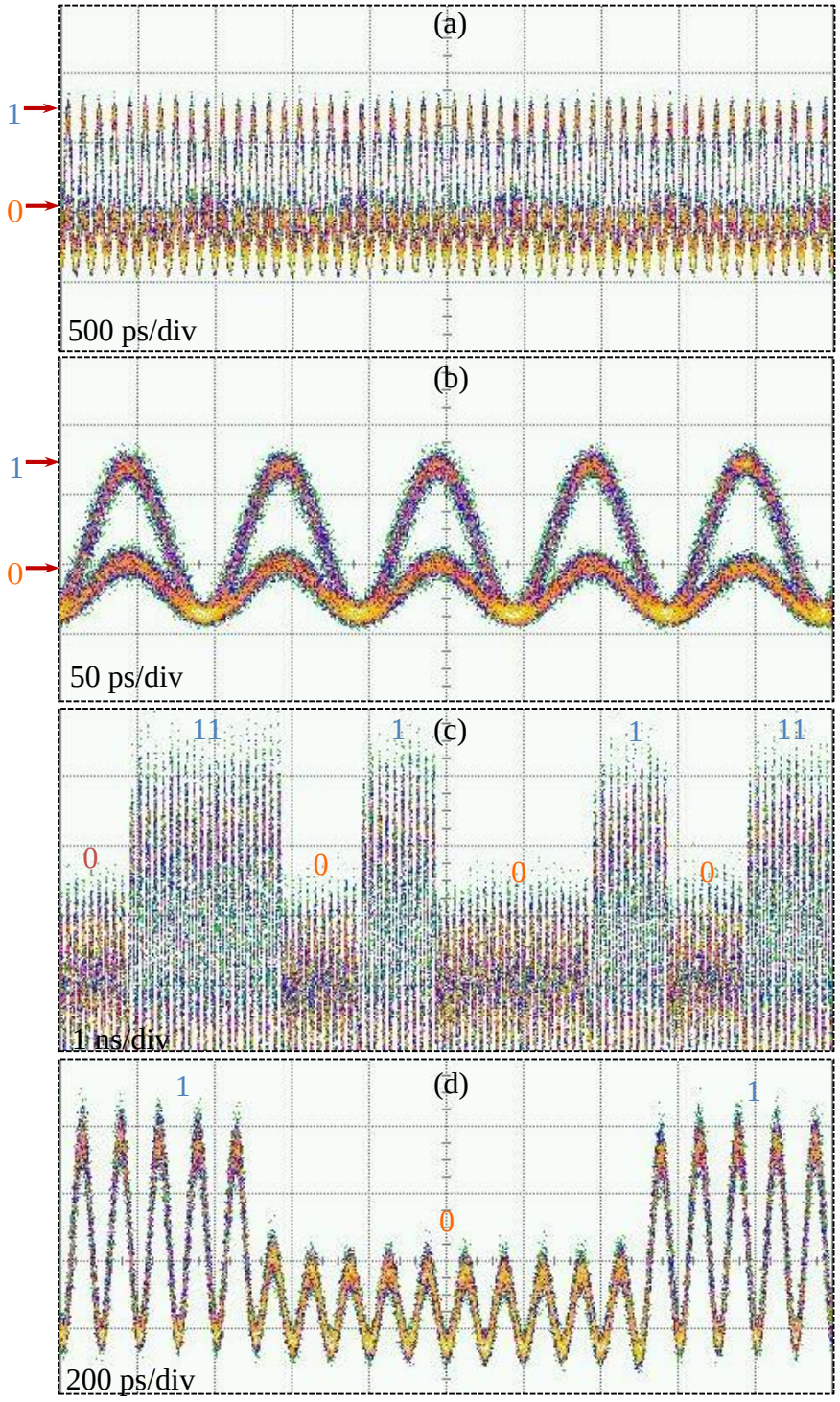

Figure 5.5. (a)-(b) Eye diagrams of PRBS ASK modulation at 1-Gbps; (c)-(d) 11010010 bit sequence ASK modulation.

Phase modulation capability is crucial to enable advanced modulation schemes for improved transmission capacity and performance. The carrier and the +1st order sideband generated in our scheme have good phase coherence between them; thus, our scheme also works well for phase modulation without the need of complex off-line signal processing for phase compensation. To perform phase modulation, the MZM for IF modulation is biased at its minimum transmission point such that a 0 phase is resulted when the modulating signal is a bit zero, while π phase is resulted when the signal is a bit 1. A 1-Gbps 2^{15}-1 PRBS signal is used as the IF for modulation. Figure 5.6(a) is a zoom-in view of the resulting eye diagram after phase modulation, which clearly indicates the 0 phase and π phase of the BPSK signal. A bit sequence with alternative 1 and 0 is used as the IF signal to observe the change in phase. Figure 5.6(b) is the waveform with the edges of the bits marked by the red arrows. During bit 0, the valley of the 10-GHz LO is aligned with

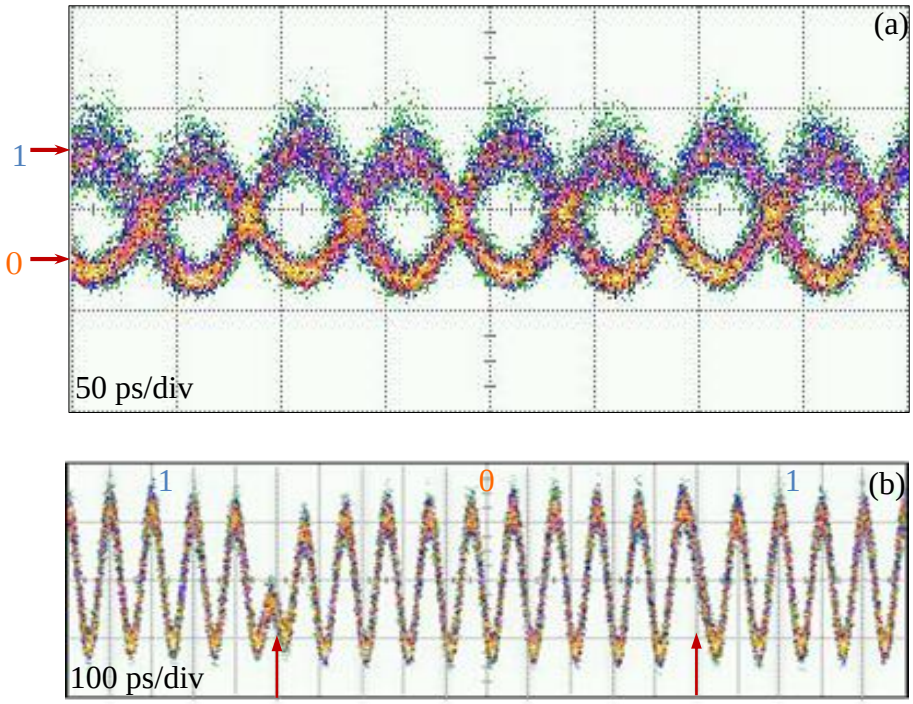

Figure 5.6. 1-Gbps phase modulation (a) Eye diagram; (b) Waveform.

the vertical grid lines, representing 0 phase; while the peak of the 10-GHz LO is aligned with the vertical grid line during bit 1, which indicates a π phase shift in the LO.

5.4 Summary

In summary, we proposed and demonstrated a microwave photonic mixer scheme that is capable for performing both amplitude and phase modulation. Our approach utilizes SSB generation in DDMZM and polarization rotation in SOA for the generation of phase coherent optical carriers. Various modulation schemes including OOK, ASK and BPSK have been implemented and verified by the resultant widely opened eye diagrams and clear waveforms. Our scheme does not have a hard limit on the supported lowest LO frequency and the LO frequency can be tunable without the need of reconfiguring the setup. Through the incorporation with the proposed microwave photonic mixer, our ICS can be able to support larger transmission capacity and obtain higher spectral efficiency.

CHAPTER 6

CONCLUSION

6.1 Summary of the thesis

This thesis describes the development of a high capacity co-site co-channel interference cancellation system and its related application for wireless communications. With the help of the high precision optical components and the smaller S21 mismatch over the whole system, this architecture offers an impressive cancellation performance over existing approaches, both electrical and optical based. A 30-dB cancellation over 5.5 GHz, 50-dB cancellation over 150 MHz are experimentally achieved for the line of sight interference, while 30-dB cancellation over 2 GHz as well as 50-dB cancellation over 40 MHz are obtained considering multipath effects. With the help of CPO effects in SOA, the interference cancellation system is able to be tuned at the GHz speed, which make it suitable for dynamic interference cancellation in a fast vibrating channel. A novel microwave photonic mixer is proposed and experimentally demonstrated to help improve the transmission capacity of the proposed architecture through its capability for advanced modulation formats.

Our proposed architecture is efficient for high capacity simultaneously transmitting and receiving. However, it's not scalable and suitable for mobile applications. To further improve this architecture, the fast growing silicon photonics community will be able to

leverage the high-bandwidth and precision of optics with small size, weight and power consumption of integrated circuits.

6.2 Future Direction

The future work are exploring the integration of self-interference cancellation system based on Si platform, and to incorporate the applications into wireless communications and more using the integrated self-interference cancellation system.

The future plan includes:

- Integrated all-optical fast tunable delay: The optically-induced change in dispersion via stimulated Raman scattering has demonstrated the efficiency to generate tunable all-optical delay. This all-optical delay can enable ultrafast adaptive reconfigurations of delay to match the dynamic wireless channel environment. The large Raman gain coefficient in silicon on insulator (SOI) waveguide and relatively narrow fabrication linewidth of silicon have significant advantages to provide large slow-light effects. The future work can be characterizing the relationship on how pump intensity, Raman frequency and length of interaction SOI waveguide affect the tunability, bandwidth and delay range of the integrated optical delay line. The SOI waveguide for all-optical delays can be easily fabricated through Si platform [42].

- Signal inversion based on integrated silicon ring resonator: The modulated pump light used as control and continuous wave (CW) probe light used as signal, tuned at two distinct resonances of the ring resonator can be coupled together into the ring resonator. When the control light power is high, the two-photon absorption (TPA) effect will cause the generation of free carriers inside the ring resonator. The transmission of the signal will change because of resonance shift. When the control light power is low, the resonant wavelength and the transmission of the signal will relax back due to the recombination of the free carriers. In this way, the RF signal modulated on the pump light will be inverted and transferred to the probe light. The dynamic process of TPA in silicon ring resonator is fast and will be able to provide a real time on-chip signal inverter [43].

Integration and fabrication of the integrated self-interference cancellation system: Future work can be incorporating all the successful designs of the previous two steps, optimize the system in a whole, fabricate it based on SOI platform and test the cancellation performance.

REFERENCE

1. Raghavan, Anand, Edward Gebara, Emmanouil M. Tentzeris, and Joy Laskar. "Analysis and design of an interference canceller for collocated radios."*Microwave Theory and Techniques, IEEE Transactions on* 53, no. 11 (2005): 3498-3508.
2. QHx220 datasheet, http://www.angliam2m.com/GPS/intersil/QHx220.pdf.
3. Dirk Slock, and Hafedh Trigui. "An interference cancelling multichannel matched filter." In *Global Telecommunications Conference, 1996. GLOBECOM'96.'Communications: The Key to Global Prosperity*, pp. 214-218. IEEE, 1996.
4. Shyamnath Gollakota, and Dina Katabi. *Zigzag decoding: combating hidden terminals in wireless networks*. Vol. 38, no. 4. ACM, 2008.
5. Mayank Jain, Jung Il Choi, Taemin Kim, Dinesh Bharadia, Siddharth Seth, Kannan Srinivasan, Philip Levis, Sachin Katti, and Prasun Sinha. "Practical, real-time, full duplex wireless." In *Proceedings of the 17th annual international conference on Mobile computing and networking*, pp. 301-312. ACM, 2011.
6. José Capmany, Beatriz Ortega, and Daniel Pastor. "A tutorial on microwave photonic filters." *Lightwave Technology, Journal of* 24, no. 1 (2006): 201-229.
7. Alexander Sonnenschein, and Warren Hutchinson. "A design for an electro-optic implementation of a wideband nulling system." In *Military Communications Conference, 1990. MILCOM'90, Conference Record, A New Era. 1990 IEEE*, pp. 742-748. IEEE, 1990.

8. John Suarez, Konstantin Kravtsov, and Paul R. Prucnal. "Incoherent method of optical interference cancellation for radio-frequency communications."*Quantum Electronics, IEEE Journal of* 45, no. 4 (2009): 402-408.
9. Matthew P. Chang, Mable Fok, Andrew Hofmaier, and Paul R. Prucnal. "Optical analog self-interference cancellation using electro-absorption modulators." *Microwave and Wireless Components Letters, IEEE* 23, no. 2 (2013): 99-101.
10. Maddie Lu, Matt Chang, Yanhua Deng, and Paul R. Prucnal. "Performance comparison of optical interference cancellation system architectures." *Applied optics* 52, no. 11 (2013): 2484-2493.
11. Matthew P. Chang, Chia-Lo Lee, Ben Wu, and Paul R. Prucnal. "Adaptive Optical Self-Interference Cancellation Using a Semiconductor Optical Amplifier." *Photonics Technology Letters, IEEE* 27, no. 9 (2015): 1018-1021.
12. Qi Zhou, Hanlin Feng, Guy Scott, and Mable P. Fok. "Wideband co-site interference cancellation based on hybrid electrical and optical techniques."*Optics letters* 39, no. 22 (2014): 6537-6540.
13. Joana Chang, and Paul R. Prucnal. "A novel analog photonic method for broadband multipath interference cancellation." *Microwave and Wireless Components Letters, IEEE* 23, no. 7 (2013): 377-379.
14. Kui Wang, Ran Tao, Yongfeng Ma, and Tao Shan. "Adaptive multipath cancellation algorithm in passive radar." In *Radar, 2006. CIE'06. International Conference on*, pp. 1-4. IEEE, 2006.

15. Paul R. Prucnal, ed. *Optical code division multiple access: fundamentals and applications*. CRC press, 2005.
16. Aldo Cassola, Tao Jin, Guevara Noubir, and Bishal Thapa. "Efficient spread spectrum communication without preshared secrets." *Mobile Computing, IEEE Transactions on* 12, no. 8 (2013): 1669-1680.
17. Xu Chang Qing, Pan Ju Yan, Zhu Jun Jie, and H. Katsuragawa. "Reduced-complexity multipath interference cancellation technique." In *Vehicular Technology Conference, 2002. Proceedings. VTC 2002-Fall. 2002 IEEE 56th*, vol. 3, pp. 1735-1738. IEEE, 2002.
18. Ji-Won Park, Seung-Hun Song, and Tae-Kyung Sung. "Interference cancellation in multipath environment for mobile WiMAX Geo-location system." In *Position Location and Navigation Symposium (PLANS), 2010 IEEE/ION*, pp. 783-786. IEEE, 2010.
19. Derong Liu, and Hossein Zare. "A multipath interference cancellation technique for WCDMA downlink receivers." *International Journal of Communication Systems* 20, no. 6 (2007): 661-668.
20. Chapman, David. "Low-loss many-to-one fiber couplers with few or single-moded inputs and a multi-mode output." *Fiber and integrated optics* 23, no. 5 (2004): 375-385.
21. Mable P. Fok, Yanhua Deng, Konstantin Kravtsov, and Paul R. Prucnal. "Signal beating elimination using single-mode fiber to multimode fiber coupling."*Optics letters* 36, no. 23 (2011): 4578-4580.

22. Niu, Yong, Yong Li, Depeng Jin, Li Su, and Athanasios V. Vasilakos. "A Survey of Millimeter Wave (mmWave) Communications for 5G: Opportunities and Challenges." *arXiv preprint arXiv:1502.07228* (2015).
23. Xia, Fengnian, Lidija Sekaric, and Yurii Vlasov. "Ultracompact optical buffers on a silicon chip." *Nature photonics* 1, no. 1 (2007): 65-71.
24. Meijerink, Arjan, Chris GH Roeloffzen, Roland Meijerink, Leimeng Zhuang, David AI Marpaung, Mark J. Bentum, Maurizio Burla et al. "Novel ring resonator-based integrated photonic beamformer for broadband phased array receive antennas—Part I: Design and performance analysis." *Lightwave Technology, Journal of* 28, no. 1 (2010): 3-18.
25. Tomohiro Akiyama, Hirofumi Matsuzawa, Eisuke Haraguchi, Hideo Sumiyoshi, Toshiyuki Ando, Akira Akaishi, Tatsuro Takahashi, Yoshiyuki Fujino, and Ryo Suzuki. "Spatial light modulator based optically controlled beamformer for variable multiple-spot beam antenna." In *Microwave Photonics, 2011 International Topical Meeting on & Microwave Photonics Conference, 2011 Asia-Pacific, MWP/APMP*, pp. 401-404. IEEE, 2011.
26. Jingya Xie, Linjie Zhou, Zuxiang Li, Jinting Wang, and Jianping Chen. "Seven-bit reconfigurable optical true time delay line based on silicon integration."*Optics express* 22, no. 19 (2014): 22707-22715.
27. S. Namiki, “Wide-band and -range tunable dispersion compensation through parametric wavelength conversion and dispersive optical fibers,” J. Lightwave Technol. 26, no. 1 (2008): 28-35.

28. Blais, Sebastien, and Jianping Yao. "Photonic true-time delay beamforming based on superstructured fiber Bragg gratings with linearly increasing equivalent chirps." *Journal of Lightwave Technology* 27, no. 9 (2009): 1147-1154.
29. Jacob B Khurgin. "Slow light in various media: a tutorial." *Advances in Optics and Photonics* 2, no. 3 (2010): 287-318.
30. Salvador Sales, Weiqi Xue, Jesper Mørk, and Ivana Gasulla. "Slow and fast light effects and their applications to microwave photonics using semiconductor optical amplifiers." *Microwave Theory and Techniques, IEEE Transactions on*58, no. 11 (2010): 3022-3038.
31. Jianping Yao. "Microwave photonics." *Lightwave Technology, Journal of* 27, no. 3 (2009): 314-335.
32. Erwin HW Chan, and Robert A. Minasian. "High conversion efficiency microwave photonic mixer based on stimulated Brillouin scattering carrier suppression technique." *Optics letters* 38, no. 24 (2013): 5292-5295.
33. Ganesh K. Gopalakrishnan, William K. Burns, and Catherine H. Bulmer. "Microwave-optical mixing in LiNbO 3 modulators." *Microwave Theory and Techniques, IEEE Transactions on* 41, no. 12 (1993): 2383-2391.
34. Yongsheng Gao, Aijun Wen, Huixing Zhang, Shuiying Xiang, Hongqin Zhang, Lijun Zhao, and Lei Shang. "An efficient photonic mixer with frequency doubling based on a dual-parallel MZM." *Optics Communications* 321 (2014): 11-15.
35. Tadao Nagatsuma, Shogo Horiguchi, Yusuke Minamikata, Yasuyuki Yoshimizu, Shintaro Hisatake, Shigeru Kuwano, Naoto Yoshimoto, Jun Terada, and Hiroyuki

Takahashi. "Terahertz wireless communications based on photonics technologies." *Optics express* 21, no. 20 (2013): 23736-23747.

36. T. Nagatsuma, S. Horiguchi, Y. Minamikata, Y. Yoshimizu, S. Hisatake, S. Kuwano, N. Yoshimoto, J. Terada, and H. Takahashi, "Terahertz wireless communications based on photonics technologies", Opt. Exp., vol. 21, no. 20, pp.23736-23747, Oct. 7, 2013.
37. Ming Zhu, Liang Zhang, Shu-Hao Fan, Charles Su, Gordon Gu, and Gee-Kung Chang. "Efficient delivery of integrated wired and wireless services in UDWDM-RoF-PON coherent access network." *Photonics Technology Letters, IEEE* 24, no. 13 (2012): 1127-1129.
38. Xinying Li, Ze Dong, Jianjun Yu, Nan Chi, Yufeng Shao, and G. K. Chang. "Fiber-wireless transmission system of 108 Gb/sdata over 80 km fiber and 2 × 2multiple-input multiple-output wireless links at 100 GHz W-band frequency."*Optics letters* 37, no. 24 (2012): 5106-5108.
39. S. Koenig, D. Lopez-Diaz, J. Antes, F. Boes, R. Henneberger, A. Leuther, A. Tessmann et al. "Wireless sub-THz communication system with high data rate." *Nature Photonics* 7, no. 12 (2013): 977-981.
40. Jianyu Zheng, Jing Wang, Jian Yu, Ming Zhu, Ze Dong, Xin Wang, Ting Su, Jianguo Liu, Ninghua Zhu, and Gee-Kung Chang. "Photonic microwave-signal-mixing technique using phase-coherent orthogonal optical carriers for radio-over-fiber application." *Optics Letters* 39, no. 18 (2014): 5263-5266.
41. Huan Jiang, He Wen, Xiaoping Zheng, Zhigang Liu, Kai Wang, Hanyi Zhang, and Yili Guo. "Improved optical single-sideband generation using the self-modulation

birefringence difference in semiconductor optical amplifiers." *Optics letters* 32, no. 17 (2007): 2580-2582.

42. Jia Ge, Hanlin Feng, Guy Scott, and Mable P. Fok. "High-speed tunable microwave photonic notch filter based on phase modulator incorporated Lyot filter." *Optics letters* 40, no. 1 (2015): 48-51.
43. Jaime Cardenas, Mark A. Foster, Nicolás Sherwood-Droz, Carl B. Poitras, Hugo LR Lira, Beibei Zhang, Alexander L. Gaeta, Jacob B. Khurgin, Paul Morton, and Michal Lipson. "Wide-bandwidth continuously tunable optical delay line using silicon microring resonators." *Optics express* 18, no. 25 (2010): 26525-26534.
44. Qianfan Xu, Vilson R. Almeida, and Michal Lipson. "Micrometer-scale all-optical wavelength converter on silicon." *Optics letters* 30, no. 20 (2005): 2733-2735.

APPENDIX

Matlab simulation code for interference cancellation system:

Fun1:

```
function[x]=fun1(a,t,w)
   x=db(abs((10^((w+a)/10)*exp(-1i*t*pi/180)-10^(w/10))))-w;
```

Fun2:

```
function[x]=fun2(a,t,w)
   x=db(abs((10^((w+a)/10)*exp(-1i*t*pi/180)-10^(w/10))))-w;

x=ones(21);
y=ones(21);
z=ones(21);
for i=1:1:21
    for j=1:1:21
        z(i,j)=fun1(10^(-2+(i-1)/10),10^(-1+(j-1)/10),-20);
        x(i,j)=10^(-2+(i-1)/10);
        y(i,j)=10^(-1+(j-1)/10);
    end
end
mesh(x,y,z)
```